5-1-2023

STUDY OF ADVANCED FRICTION MATERIAL FOR THE AUTOMOTIVE INDUSTRY

Manisha Upreti
Southern Illinois University Carbondale, manishaupreti80@gmail.com

Recommended Citation

Upreti, Manisha, "STUDY OF ADVANCED FRICTION MATERIAL FOR THE AUTOMOTIVE INDUSTRY" (2023). *Theses*. 3100.
https://opensiuc.lib.siu.edu/theses/3100

STUDY OF ADVANCED FRICTION MATERIAL FOR THE AUTOMOTIVE INDUSTRY

by

Manisha Upreti

B.E., Mechanical Engineering, Kathmandu University, 2020

A Thesis
Submitted in Partial Fulfillment of the Requirements for the
Master of Science Degree

School of Mechanical, Aerospace, Materials Engineering
in the Graduate School
Southern Illinois University Carbondale
May 2023

THESIS APPROVAL

STUDY OF ADVANCED FRICTION MATERIAL FOR THE AUTOMOTIVE INDUSTRY

by

Manisha Upreti

A Thesis Submitted in Partial

Fulfillment of the Requirements

for the Degree of

Master of Science

in the field of Mechanical Engineering

Approved by:

Dr. Peter Filip, Chair

Dr. Rasit Koc

Dr. Sangjin Jung

Graduate School
Southern Illinois University Carbondale
March 31, 2023

AN ABSTRACT OF THE THESIS OF

Manisha Upreti, for the Master of Science degree in Mechanical Engineering, presented on March 31, 2023, at Southern Illinois University Carbondale.

TITLE: STUDY OF ADVANCED FRICTION MATERIAL FOR THE AUTOMOTIVE INDUSTRY

MAJOR PROFESSOR: Dr. Peter Filip

Manufacturing/casting defects and the corroding nature of grey cast iron require the attention of researchers to search for a better alternative to grey cast iron rotors. The increasing demand and market of electric, hybrid vehicles draw the attention of scientists and car manufacturers to conduct more research to find suitable and sustainable braking material that can overcome the issues related to grey cast iron rotors brakes. A modern alternative for grey cast iron rotors may be 3D-printed stainless steel rotors. The promising future of 3D printing technology has propelled the manufacturing industry into a new era of customized fabrication. Thus, choosing 3D printing technology which can automate the manufacturing of rotors could be a good alternative to address the manufacturing defects related to grey cast iron rotors. Also, with a paradigm shift with regenerative braking, there is a need for a lightweight, non-corroding brake that can replace regular cast iron rotors. The goal of this research is to address the friction performance of the brake system with an NAO commercial pad and laboratory 3D-printed stainless steel brake rotor. The friction testing was conducted using a scaled-down ISO/SAE J2522 procedure on a benchtop friction tester (Brucker UMT) equipped with an environmental chamber controlling temperature. The relative humidity was kept at a constant value of 50%. Scaled-down samples were manufactured from commercially available NAO brake pads with a diameter of 13 mm were rubbed against rotors with a diameter of 90 mm. The friction and wear mechanisms were studied by analyzing the surfaces of tested pads and rotors using scanning electron microscopy in secondary and backscattered electron modes (SEM, Quanta FEG 450 by FEI). The results showed that a more stable and smooth friction layer was formed on stainless steel rotors (R_a=1.2 μm). This was responsible for a very stable and high friction level detected in systems with 3D printed rotors (average $\mu \sim 0.4 \pm 0.1$). Wear of the 3D printed rotor was measured after completion of the entire procedure and was extremely low (avg 0.28 g). However, the wear of NAO pad was high (avg 0.9 g). Noise generated during section 4.5 speed/ pressure sensitivity of SAEJ2522 for the stainless-steel rotor was high with a maximum noise level of 108 dBA. A further study of friction performance of 3D printed stainless-steel rotors is recommended to better understand its suitability for its commercial applications.

ACKNOWLEDGMENTS

I would like to express my sincere gratitude to my advisor Dr. Peter Filip, for his invaluable guidance and support throughout the research work. His expert advice, constructive feedback, and patience were essential in shaping this research work and bringing it to completion. I am truly grateful for his mentorship and unwavering commitment to my academic success.

I would like to thank my committee member Dr. Rasit Koc, and Dr. Sangjin Jung, for their immense support and guidance while writing the thesis.

I would also like to extend my thanks to Sai Krishna Kancharla and Vishal Singireddy for their contributions to successfully completing this research work. Their insightful discussion, constructive criticism, and encouragement were instrumental in shaping my ideas and refining my research. Their friendship and support made this journey enjoyable and meaningful.

Finally, I would like to thank my family and friends for their unwavering support and encouragement throughout my academic journey. Their love and encouragement have been a constant source of motivation, and I am grateful for their unwavering belief in me.

TABLE OF CONTENTS

LIST OF FIGURES

LIST OF TABLES

CHAPTER 1

INTRODUCTION

Friction is the process that imposes resistance to the relative motion of two surfaces in contact. The friction force highly depends upon the material friction properties, surface roughness, and texture [1] . When two surfaces in motion are rubbed against each other, friction force comes to play and stops or decelerates the vehicle. This occurs as the vehicle's kinetic energy is transformed into heat energy and dissipated into the surrounding environment. The automotive industry has been using friction force to stop the rotational motion of the automobile for decades. It is called friction braking systems and they are primarily used in most IC engine, hybrid, and electric automotive vehicles. There are different types of braking systems among which disc brake systems and drum brake systems are widely popular [2].

In modern automobiles, disc brakes are primarily used. There are two components in the disc brake system, i.e.: the brake pad and brake rotor as shown in Figure 1. As brake pads are pressed against the rotor surface, the vehicle decelerates [3]. The sliding surface of the brake pad on the disc/ rotor is called brake lining and is sometimes also referred to as the consumable part. Commonly used brake lining before the 1870s was cast iron on steel and they were primarily used for railroads [4]. Later in 1908, the use of woven asbestos with brass and other wire in automobiles and trucks increased its strength and performance. Similarly, glass fibers, resin binders, mineral fibers, metal fibers, and carbon and synthetic fibers with metallic material were used to get a high performance than asbestos brake pads [5]. Also, concerning the hazardous issue related to asbestos brake pads, the use of such brake pads was discouraged in 1920. Since then, the application of non-asbestos, fiberglass, and materials brake pads were popular in the automotive industry [6].

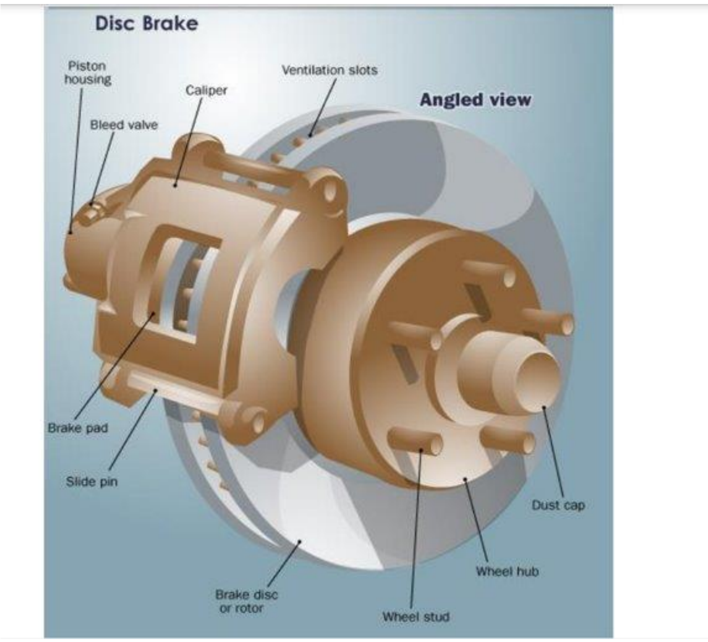

Figure 1: A schematic of disc brake [2]

To manufacture a brake pad, an average of 10 to 20 different materials are used [7]. To get the required braking in any given operating condition, a decision must be considered regarding the material selection. Brake pads are classified based on friction material used as, semi-metallic, non-asbestos organic (NAO) or ceramic, low metallic, and carbon-carbon [7], [8].

NAO brake pads are made up of organic material reinforced with aramid, glass, or ceramic, carbon, copper, and steel fibers. NAO brake pads are nonhazardous to health, and they are highly durable, resistant to high temperatures, low wear, and quiet in operation [6].

Pearlitic cast iron is a commonly used material to manufacture disc rotors and SAE has maintained a specification for manufacturing grey iron for various applications. SAE specification J431 G3000 is recommended for passenger cars and light truck applications [9]. According to the application of brake rotors, different materials are used. Cast iron usually refers to as gray cast iron is a ferrous alloy. Cast iron is made up of an iron content of 95%, carbon content of 2.1 – 4%, and silicon content of approximately 1- 3%. Also, graphite flakes are present in the gray cast iron. The typical composition of gray cast iron rotor is fully pearlitic gray cast iron and 2-4 vol/ % of free ferrite[3], [7], [10]. Since ferrite, cementite lamellae, and graphite flakes are abundantly present in gray cast iron, it has high thermal conductivity or diffusivity [10]. The higher the graphite content, the higher the thermal conductivity, and vice versa [7]. Similarly, the damping capacity of an alloy can be maximized by increasing its graphite content. The results of a study conducted on the damping behavior of ZA-27 alloy composite material investigating the impact of graphite particles indicated that an increase in temperature and the proportion of graphite particles led to a corresponding increase in the material's damping capacity [11].

Testing is a crucial step in evaluating the efficiency of brakes, following the manufacturing of brake pads and discs. A range of tests, including on-field tests, laboratory tests such as dyno, and other small-scale tests help to assess the brake pad and rotor. However, the ultimate evaluation is carried out through vehicle tests that utilize full-sized components. Laboratory wear methods do not fully replicate the real dyno tests but help researchers to correlate the laboratory results to the full-scale dyno application [2]. ASTM has developed multiple testing methods, such as ASTM G99 which uses pin-on-disk apparatus to measure wear. In contrast, ASTM G133 uses a linearly reciprocating ball-on-flat-sliding apparatus for wear. However, ASTM G115 is for gauging the coefficient of friction. However, it may not be immediately apparent how to select the appropriate equipment and accurately simulate practical operating conditions when utilizing these methods [12]. Several other researchers also fail to find a correlation between the coefficient of friction (COF) value obtained for different testing methods [3].

To address variations in testing methodologies and to adapt full-scale dynamometers for use in small-scale testing, it may be beneficial to explore the law of scaling based on principles of physics. This approach involves utilizing a scaling philosophy to effectively adjust. Testing parameters, such as time, sliding speed, and normal load are adjusted effectively utilizing a scaling philosophy. However, since temperature and deceleration cannot be scaled-down, identical values should be utilized instead [12]. To replicate the heat generated during the braking, an external heating chamber shall be used that helps to maintain the required temperature at a different phase of friction testing.

Although the scaling and the related test do not completely predict friction performance in real-life applications, it helps to make an educated decision, specifically in the “research and development stage”. In addition to normal load, sliding speed, and time, the performance of a given “friction system” is greatly influenced by its stiffness and damping characteristics. Moreover, environmental conditions, humidity, and temperature play a crucial role in friction performance [2].

The goal of this research is to explore new friction materials for modern-day automobiles specifically electric vehicles where brake disc corrosion is a major challenge. It deals with the investigation of the effectiveness of 3D-printed stainless-steel rotors in terms of wear, coefficient of friction, and noise study.

In this research, the friction performance, coefficient of friction, and wear, of stainless-steel rotors with laboratory-fabricated NAO brake pads were verified using SAE J2522 testing standards. The test is conducted in the benchtop UMT (Universal Mechanical Tester) in a constant humidity where the wear of the brake pads and rotors was analyzed before and after the UMT test. Also, the level of coefficient of friction during different stages of SAEJ2522 shows the effectiveness of the brake pad and rotor. However, small-scale bench testers cannot deliver enough heat generated due to friction required during fade and temperature/pressure sensitivity sections compared to full-sized automotive brake dynamometers. Hence to resolve this issue, a custom build heating chamber by Brucker was used to meet the required heating in small-size bench testing. Also, Scanning Electron Microscopy (SEM) and Energy-dispersive X-ray spectroscopy (EDX) analysis were used for studying the developed friction layers.

Gray cast iron rotors, although have high thermal conductivity, have a few drawbacks like corrosion and this is the major challenge Electric Vehicles (EVs) face these days. In the case of high and low speed / emergency braking, regenerative braking is not sufficient to provide the required braking. At this point, the friction brake comes into play. However, if the brake disc is corroded, it cannot provide the desired braking which may lead to fatalities. Therefore, there is a need for an alternative brake disc that can mitigate this issue. As stainless steel is less corroding and lightweight, it can be used as an alternative brake pad to address the issue of corrosion.

CHAPTER 2

LITERATURE REVIEW

Friction braking is a type of braking mechanism that relies on friction between two surfaces to slow down or stop a moving object. It is achieved by pressing brake pads against a rotating surface such as a wheel or rotor, generating friction, which slows down or stops the rotation. The two main types of friction braking systems are:

1. Drum Brakes: It comprises a rotating drum attached to a wheel and a set of brake shoes that apply pressure to the interior surface of the drum in order to stop the wheel's rotation. When the brake pedals are activated, hydraulic fluid flows from the master cylinder to the brake shoes in drum brakes, which then expand and apply pressure to the drum. Although drum brakes are less frequently used in contemporary vehicles, they can still be found on some older models or cost-efficient vehicles [13].

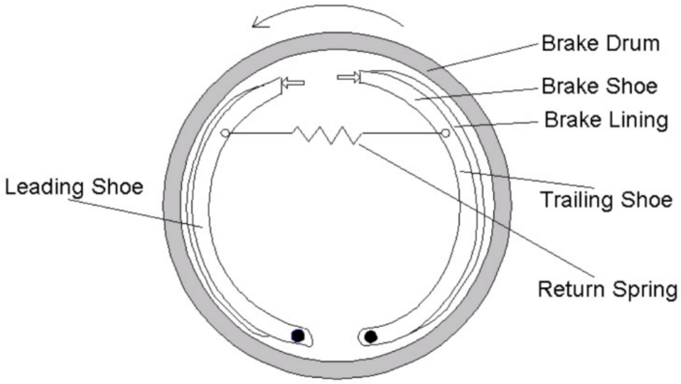

Figure 2: A schematic of drum brake [14]

2. Disc Brakes: Discs brakes are comprised of a rotor that spins along with the wheel and a caliper holding the brake pads. When force is applied on the brake pedal, force is transmitted to the caliper causing the brake pads to clamp down on the rotor resulting in the stopping of the vehicle. The force from the pedal is transmitted to the caliper through the actuator [13]. There are three types of actuating systems, mechanical, pneumatic, and hydraulic actuators. The mechanical actuation system uses rods and cables to transmit the force applied to the brake pedal to the brake pads. Hydraulic actuation systems are more efficient than mechanical actuation systems. The hydraulic actuation consists of hydraulic fluid transmitting force from the brake pedal into brake pads/ shoes. The applied force is converted into hydraulic pressure with the help of the master cylinder present in the disc brake system. The hydraulic fluid is carried from the master cylinder to brake shoes through brake lines or brake pipes. As force is applied to the master cylinder using the brake pedal, it increases the pressure of the hydraulic fluid in the brake lines. This increased pressure is transmitted to the brake calipers or brake pads resulting in the pressing of the rotor to stop or slow down the vehicle. The hydraulic braking system gives consistent and smooth braking responses, and they are reliable to handle the high braking forces generated by modern vehicles [3].

2.1 Classification of brake pad

Brake pads are classified based on the materials used for the brake lining. Semi-Metallic, Low-Metallic, Non-Asbestos Organic, Sintered Metallic, Ceramic Matrix Composites, and Carbon-Carbon Composites [7].

Semi-metallic brake pads are manufactured using a mixture of metallic and non-metallic materials. Steel fibers, iron powder, copper, and composite alloys are used as metallic components of the brake pad whereas synthetic materials like glass fibers, rubber, and resins are the non-metallic components of the brake pad. [1]. Semi-metallic pads are affordable compared to ceramic brake pads which makes them an alternative option for budget-conscious vehicle owners. Similarly, the good heat dissipation quality of metals helps to reduce the brake fade and improve overall braking performance. However, due to metallic components, they tend to produce more noise and dust compared to organic pads and the abrasive action of the metallic component of the pad potentially damages the rotor [7].

Low metallic brake pads were introduced in the 1960s and have a lower percentage of metallic components compared to the metallic brake pad, hence resulting in less dust and noise. Asbestos in brake pads was introduced around 1908 and was widely used till the 1990s. However, due to the health hazards factor of asbestos, they were banned from application in the late 1980s [3]. Later Non-asbestos organic (NAO) brake pads were introduced.

NAO brake pads are made of 50-90% resins, 5-25% aramids fibers, 2-15 % carbon, and 2-15% fillers [7]. Aramid fibers like Kevlar, a type of synthetic polymer, is used in such pad. They provide high strength and heat resistance. The application of graphite in pad material improves their heat dissipation capacity and reduces brake fades. Resins like phenolic and phenol-formaldehyde are used as binding material and fillers such as glass fibers in NAO brake pads improve their dimensional stability and reduce brake noise [1], [7].

Sintered metallic brake pads were introduced in the 1950s [3] and are made from a mixture of sintered, or melted and molded, into solid brake pads. A mixture of copper, iron, and other metals is used as they are known for their durability, heat resistance, and consistent braking performances. However, they are not as quiet as other brake types and produce more dust and noise [7].

Ceramic matrix composite (CMC) brake pads are made of ceramic materials reinforced with fibers, such as carbon or aramid fibers [1], [7]. These brake pads have low weight and low dust emissions. Carbon-carbon composite (CCC) brake pads are made from a mixture of carbon fibers and a carbon matrix and are commonly utilized in high-performance fields such as motorsports, aerospace, and military [1]. They are chosen for their remarkable ability to withstand high temperatures and their long-lasting nature. These brake pads are ideal for those who demand exceptional performance in challenging driving conditions, but it’s crucial to weigh the potential downsides, such as cost and increased wear on rotors and brake dust [7].

2.2 Classification of brake material

Based on the functions, the brake materials and additives can be categorized as follows [1]:

1. Friction Modifiers
    a) Abrasive
    b) Lubricant
2. Fillers
3. Reinforcements
4. Binder Materials

Abrasive plays a role in keeping the surfaces in contact clean and managing the accumulation of friction films. In addition, they boost friction, particularly during the onset of braking, thereby supplying greater traction. Aluminum oxide, iron oxides, quartz, silica, and zirconium silicate are examples of abrasive materials[1]. Friction modifiers can either enhance or decrease the level of friction, depending on the desired performance of the brake systems [6]. Friction modifiers in brake linings include graphite, molybdenum disulfide, metal fibers, glass fibers, polytetrafluoroethylene (PTFE), and various other organic and inorganic materials [1].

Different forms of friction modifiers, such as metallic or organic substances, can be used and the amount added can significantly impact the brake’s function [6]. Some common metallic friction modifiers are copper, iron, and molybdenum disulfide as well as organic compounds like graphite, molybdenum dithiocarbonates, and other polymer materials [1].

Commonly used fillers and reinforcements are metals, alloys, ceramics, or organic materials. Fillers aid in enhancing the mechanical characteristics and thermal conductivity of the brake pad. Binders in brake linings serve the purpose of holding the abrasives, friction modifiers, and fillers in place. These materials work to maintain the brake pad’s structural stability even under high stress and heat [6]. Binders can be made from various substances, like resins, oils, and waxes are chosen based on the brake systems’ needs, such as thermal resistance strength, and hardness. Typical binder materials employed in brake systems include phenolic resin, metallic alloys such as copper iron, and nickel, and modified resins like epoxy, cashew, and rubber[1].

2.3 Brake rotor

The conventional material used for making automotive brake rotors is pearlitic gray cast iron. This material is cost-effective, easy to manufacture, and has good thermal stability, making it a popular choice for brake applications [3]. During the production of cast iron rotors, the casting procedure must be meticulously monitored to regulate the configuration, arrangement, and structure of the overabundance of carbon precipitates, thereby reducing deformation and guaranteeing favorable wear attributes [15]. Alternative materials such as titanium alloys and aluminum-metal Matrix Composited (AMC) are also being explored for brake rotor applications [16]. These materials are lighter and have better thermal conductivity, making them suitable for weight reduction in brake systems. However, they face challenges such as inhomogeneous distribution of particles, low ductility and a lack of solid lubricants. A study by of abrasive wear resistance of AA6061 with 20 % SiC reinforced composite showed that adding SiC particles improved the wear resistance and high-temperature strength of the composite, but also reduced its ductility and resulted in low product liability [17].

Potential materials for automotive brake rotors have been selected based on their properties which include [16].

1. Gray cast iron
2. Titanium alloys (Ti-6Al-4V)
3. 7.5 wt% WC and 7.5 wt% TiC reinforced Ti-composite (TMC)
4. 20% SiC reinforced Al-composite (AMC 1)
5. 20% SiC reinforced Al-Cu alloy (AMC 2)

A brake rotor made from a composite of aluminum, SiC, and graphite was developed and has been found to have improved wear resistance compared to a cast iron rotor. Likewise, the incorporation of 10% SiC and 5% nickel-coated graphite particles into an aluminum-silicon alloy matrix enhances its wear resistance. However, it also causes significant manufacturing issues [17].

Stainless steel can be used as a brake rotor as it possesses resistance to corrosion and can withstand high temperatures generated during braking. This makes it a good substitute for conventional gray cast iron rotors. Additionally, cast iron rotors are frequently heavier than stainless steel rotors, which improves the vehicle's overall weight distribution and may increase fuel efficiency. However, SS316-type stainless steel could be more favorable compared to hardness, density, thermal conductivity, and corrosion resistance. Stainless steel could not be as strong and durable as cast iron, and it might also be more expensive.

2.4 Regenerative braking

In internal combustion engine vehicles, the hydraulic braking system is used for stopping the vehicles. However, in the case of electric vehicles or hybrid vehicles, regenerative braking comes into play. Whenever the driver steps into the pedal, the electric motor acts as a generator driven by axle/ wheels and converts the rotating motion of the vehicle, kinetic energy, into electrical energy. This allows for charging batteries [18]. This is the basic principle behind regenerative braking. Electric Vehicles (EVs) are equipped with a motor (Induction or DC Brushless motor) and battery source. Lithium-ion batteries are the most used battery type in EVs [3]. A combination of regenerative and friction braking is used in hybrid and electric vehicles [18]. Moreover, additive braking and blended braking are used in hybrid and electric vehicles [19], [20]. Both braking techniques use a combination of friction and regenerative braking. In additive braking, friction braking produces most of the braking torque whereas regenerative braking produces most of the braking torque in a blended braking system. To control the amount of applied regenerative and friction braking, a brake control unit is employed in hybrid and electric vehicles [3].

2.5 Classification of additive manufacturing

Additive manufacturing is a technologically sophisticated process that employs digital information from 3D computer-aided design (CAD) to create three-dimensional (3D) objects by layer-by-layer addition of material [21]. This manufacturing process is unlike the conventional manufacturing process, where material removal or an energy-intensive process such as machining, casting, and forging is common. Additive manufacturing can produce a complex-shaped object as a single object using 3D CAD models [22].

The additive manufacturing process can be classified into 7 groups, namely: powder-bed fusion, directed energy deposition, sheet lamination, material extrusion, binder jetting, material jetting, and vat photopolymerization [21].

2.5.1 Powder-bed-based process:

Based on the source of energy, electron beam or laser beam, used during manufacturing, this process is further divided into direct metal laser sintering (DMLS), electron-beam melting (EBM), selective heat sintering (SHS), selective laser melting (SLM), and selective laser sintering (SLS) [23], [24]. In the DMLS process a power source such as a laser is used to bind material together, without melting to create a solid structure defined by a 3D CAD model of the part [22]. Whereas in EBM, an electron beam are generated using an electron-beam gun and the generated electron beam is used as a heat source. Heating of tungsten filament to an extremely high temperature releases electrons; using electric field released electrons are accelerated and then focused with electromagnetic coils. These focused beams of electron are used as heat source to melt each layer of the metal powder to the desired geometry in a vacuum. Steel and titanium alloy are two material that are extensively used in this process [25].

SLS is a type of powder-bed-fusion technology where the material powder is spread in the bed followed by compaction [21]. The laser beam, guided by a CAD program, scans the surface of the powder bed to form layers of the desired material. This process is repeated until the final product is built, layer by layer. Wax, paraffin, polymer-metal powders, steel alloys, polymers, nylon, and carbonates are the common materials used in this technology [26]. Whereas with SHS thermoplastic powder is used as its working material. In this technology, the heated building platform builds up the parts, where the roller spread across the plastic powders in layers [21]. SLM uses the same process as SLS, without full melting and fusing of material like SLS. The powder material is spread over the building platform and layers are formed using a scanning laser beam. Common materials sintered using this SLS are Steel, titanium, aluminum, cobalt-chromium, and nickel alloys.

2.5.2 Direct energy deposition:

DED uses a powerful energy source and a flow of raw materials that come together at a specific point, often under the protected inert gas. This highly dense point melts the materials, forming a melted pool. Based on a melt DED, it can be further subcategorized as laser-based DED, electron-beam DED, plasma-based DED, and electric arc-based DED. The most commonly used DED technique is the metal DED technique, where a laser beam is predominantly used as a heat source [27].

2.5.3 Sheet Lamination and Metal Extrusion

This manufacturing process uses metal sheets or paper as a manufacturing material. The layers of either metal or paper are joined together either by welding ultrasonically or by using an adhesive material to fabricate layers of CAD-model parts. The types of this additive manufacturing process are, namely: ultrasonic additive manufacturing (UAM) and Laminated object manufacturing (LOM) [22]. In the metal extrusion technique metal is forced through a shaped die to create the appropriate profile. It is an effective and continuous process for creating lengthy, uniform pieces with a constant cross-section. A billet, which is a cylindrical piece of metal, is heated at the beginning of the process until it turns plastic. The finished item is created by pushing the billet through the shaped die while it is inside a container known as a casing using a ram. After cooling and being cut to length, the extruded product may also go through extra processing, such as heat treating or surface finishing. Pipes, rods, and other goods are frequently made via extrusion [24].

2.5.4 Binder Jetting and Material Jetting

In binder jetting the jet of liquid binder binds the power material spread in the powder bed to fabricate the desired parts. Strategical jetting of drops of binder in binder jetting binds the material together [28]whereas in material jetting the material is jetted. Material jetting follows 2 patterns either a drop on demand (DoD) or a continuous manner while oriented and the application of ultraviolet rays hardened the part and the product is manufactured layer upon layer [23].

2.5.5 VAT photopolymerization

The photopolymerization process used light to cure or solidify a liquid polymer into a solid material. Most photopolymers are cured using the ultraviolet (UV) range of wavelength, but some with visible light systems. In the Vat photopolymerization technique, a liquid photopolymer resin contained in a vat is cured using a light source. The resin is typically poured into a VAT, and a light-sensitive layer is created on top of it. The resin is subsequently cured, solidifying the layer, using a light source. This process is commonly used in 3D printing and is known as stereolithography (SLA) [29].

2.6 Significance of additive manufacturing in the brake industry

Additive manufacturing and 3D printing technology have been developing rapidly for a few decades and hold great potential for the future development of the manufacturing industry [30] . Due to the paradigm shift in the manufacturing process, this technology has a huge demand in almost every manufacturing industry. Unlike traditional manufacturing processes, the 3D printing/additive manufacturing process enables to produce the parts and products that are more efficient in terms of time, money, and quality.

Commonly used brake rotors in the automotive industry are made using a traditional manufacturing process like casting and forging. Although the casting process is cost, time efficient, and easy to manufacture, the defects related to casting cannot be ignored. Porosity, cracks, shrinkage, wrapping, cold shut, and misruns are commonly found defects in casting [31].

Cast iron brake rotors are dominantly used in Internal Combustion Engine (ICE) vehicles is used to manufacture these rotors on a large scale. To overcome these shortcomings of casting defects, additive manufacturing (AM) can be used as an alternative manufacturing technique. AM can be used for large-scale and autonomous production of the desired part and products which cannot be achieved using traditional manufacturing processes like casting [21].

2.7 Scaled-down friction testing.

To overcome the challenges, related to on-vehicle field tests, industries, and researchers are working towards the development of friction brake testing equipment (eg: inertia brake dynamometer) and standardized procedure (SAE J2522) which helps to gauge the effectiveness of new friction materials under different driving scenarios [3, 32]. In full-scaled friction tests, brakes are tested at different pressure, temperatures and speeds to access their effectiveness as a brake material [33]. Although the inertia brake dynamometer was an effective tool for the evaluation of friction material, their operating cost challenged industries and researchers to develop scaled-down testing instruments that can accelerate the testing and analysis process during the development of new friction materials [3].

Various sub-scale testers like the friction assessment and screening test (FAST) machine, the Chase machine, and the pin-on-disk tester [33], [34] are utilized to screen friction material composition prior to full-scale inertia dynamometer tests. Although these sub-scale tests were economical for prescreening, the generated results could not be effectively correlated with field tests and inertia dynamometers [3]. A study conducted by Filip and Lee demonstrated no correlation between the results obtained on the full-scale dynamometer and the FAST machine [35]. Similarly, a study by [36] on the wear of brake components showed that the results of wear data from the FAST machine and full-scale dynamometer cannot be correlated. From these results, it was clear that these sub-scale testers do not follow the proper scaling law of physics, hence the results could not be correlated with full-scale brake testers [3].

Since friction is based on tribo-system properties, a proper selection of testing conditions like load, motion types, material, speed, and environment is required [3]. Proper scaling of load, area, torque, and speed should be done to get precision in the results. A study by Alnaqi et al. [37] evaluated the thermal performance results of full-scale and scaled-down testing using an inertia dynamometer and found that scaling the test based on area gives a result, which allows correlating of small-scale tests with the full-size automotive brake dynamometer.

2.8 Scaling

Scaling based on geometry helps to mitigate the difference in testing methods and effectively adapt full dynamometers to the small-scale tester. Scaling helps to simulate actual braking conditions on a small scale, and it is based on law of physics. Two types of Euclidean geometry are (a) Uniform scaling and (b) non-uniform scaling.

Uniform scaling follows the linear transformation. For example, while scaling the 2-Dimensional rectangle ABCD, if the length AB, x, is half, then the breadth AD, y, is also reduced by half. Then the area is reduced by ¼. Here scaling follows the general rule called “square law”.

$$Area\ of\ rectangle\ ABCD = Length * \ breadth \ldots\ldots\ldots\ldots\ldots\ldots (1)$$

$$Area\ of\ rectangle\ ABCD = x * y \ldots\ldots\ldots\ldots\ldots\ldots\ldots\ldots (2)$$

After scaling down the length and the breadth of the rectangle ABCD by half then

$$Area\ of\ sacled\ down\ rectangle = \frac{x}{2} * \frac{y}{2} \ldots\ldots\ldots\ldots\ldots\ldots\ldots\ldots (3)$$

$$Area\ od\ scaled\ down\ rectangle = \frac{xy}{4} \ldots\ldots\ldots\ldots\ldots\ldots\ldots\ldots (4)$$

Hence the scaling factor for the area of rectangle ABCD is 1/4 if the scaling factor for the length is ½ [3]. However, in non-uniform scaling, not every dimension is scaled down. Hence this may result in a change in the shape of the geometry before scaling. A similar approach is employed for scaling of 3-Dimensional objects. In uniform scaling, a similar approach like 2-D uniform scaling is followed. For example for a cuboid if its length, breadth, and height are halved then the surface area of the cuboid will be scaled down by ¼ and the volume would be scaled down by 1/8 [3]. Similarly, the scaling factor or area or volume may vary if this same cuboid is scaled using non-uniform scaling. It will depend upon the 3 dimensions of length (l), breadth (b), and height (h) and their scaling factors. In the case of non-uniform scaling, a general dimension, D (characteristics dimension) could be used for the determination of the scaling factor. Based on the ratio of any characteristics dimension (length, area, volume) scaling factor, λ, is determined. Scaling factor for length, L is given by

$$\frac{D1}{D2} = \lambda \qquad \text{..(5)}$$

The scaling factor for Area A is given by [3].

$$\frac{D1^2}{D2^2} = \lambda^2 \qquad \text{..(6)}$$

Similarly, other dimensions like mass, acceleration, and force can be scaled using a similar approach. In the case of scaled-down fiction testing

$$\frac{Area\ of\ actual\ brake\ pad}{Area\ of scaled\ pad\ smple} = \left(\frac{Length\ of\ actual\ brake\ pad}{Length\ of\ scaled\ brake\ pad}\right)^2 = \lambda^2$$

Parameters	**Scaling factor**
Force (N)	λ^3
Velocity (meter/sec)	$\lambda^{0.5}$

Time (sec)	$\lambda^{0.5}$
Angular velocity	$\lambda^{-0.5}$
Energy (J)	λ^{4}

Table 1: Scaling in different parameters

CHAPTER 3

EXPERIMENTAL

In this research work, industry-standard non-asbestos organic brake pad samples were developed in the laboratory using the manufacturing process based on weighting the constituent and post-curing. After the completion of these steps, the laboratory-manufactured samples are subjected to friction testing. One brake pad sample were tested with three different 3D-printed stainless-steel rotors. The efficiency of the tested samples is then analyzed based on friction performance, material properties, and wear resulting in the production of the optimized sample.

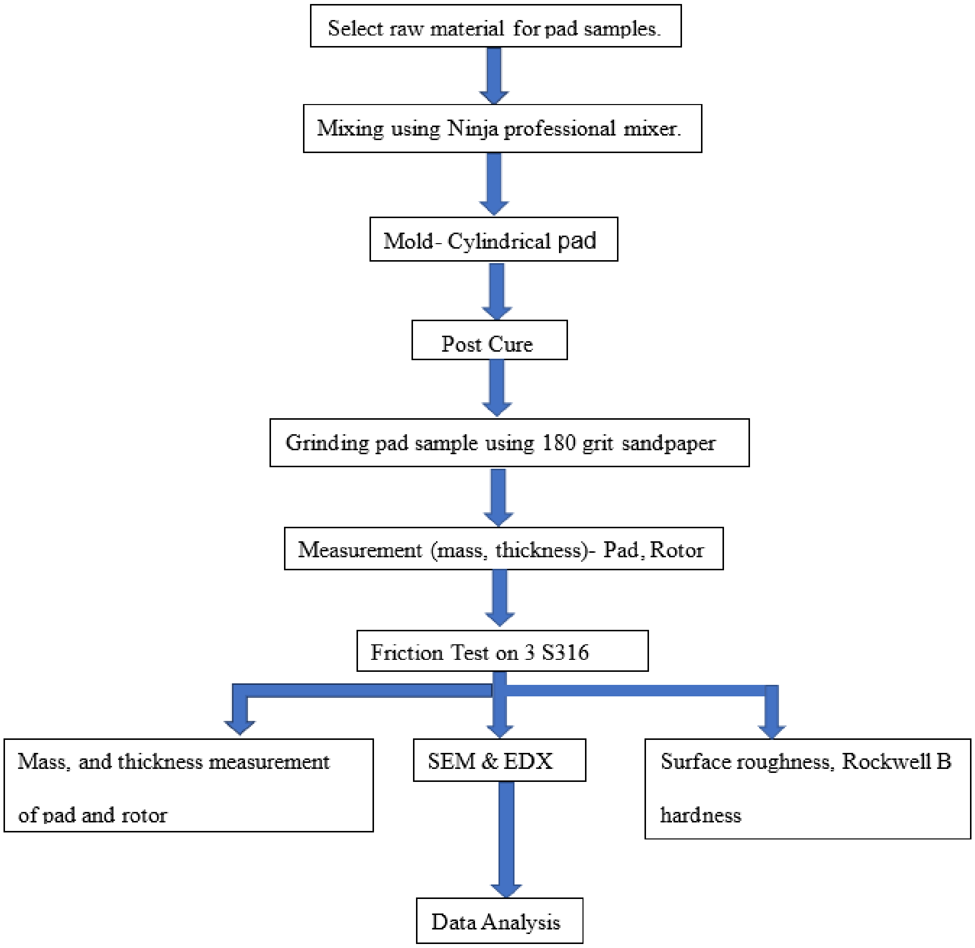

Figure 3: Research flowchart

The sample manufacturing process starts with the formulation of the brake pad. Each material was measured using an analytical balance AWS ALX-310 with an accuracy of 0.01g. in the required proportion and mixed well in a Ninja professional mixer equipped with a 1000W power motor (shown in Figure 2). 10 g of properly mixed material was then used for molding to prepare the cylindrical with samples of 13 mm diameter of equal height.

Figure 4: Ninja professional mixer [3]

The NAO brake pad samples formulated for this research work consist of brake materials like binders, fillers, fibers, abrasives, and other friction modifiers. These materials were chosen based on the findings of previous author works. Cff - fibrillated fiber (dry) is used as a binder in pad samples as it gives high thermal stability and protects pads from abrasion due to high temperature during braking. Iron oxide powder and zirconium silicate are used as abrasives as they give excellent mechanical strength and have a high coefficient of friction (μ). Similarly, 80-mesh crumb rubber, mechanomade are used as friction modifiers whereas Lapinus is a mineral fiber used in the pad formulation that reinforces the pad lining, improves the friction performance ensures stable friction film, and gives mechanical strength to the brake pad. To lower the hardness and braking noise of the pad lining calcinated petroleum coke is used in the formulation.

These brake materials were mixed in a separate batch using a ninja professional mixer with different percentage ratios. The 12 g of this mixer was used to formulate a 1” brake pad sample using Buehler mounting press. The formulated pad samples post curing as shown in Figure 6 are then tested with the S316 SS rotor.

The molding of the pad sample was carried out using a vertical mounting press, Buehler Simpliment 2, shown in Figure 5 equipped with a heater. The sample in the heater is held at a constant temperature of 170 C and mold pressure of 28.958 Mpa. The molding process is carried out in 5 cycles. For the first 4 cycles, the sample is pressed for 60 sec and the mold is released for 10 sec so that the gases generated during curing can be partially released. After these 5 cycles of pressing and releasing, the sample is taken for post-curing in a programmable Isotemp muffle furnace shown in figure 6. The sample is heated to the curing temperature of 180 C and held for 1 hr with a following cool-down process of 30 minutes. These cured samples were core drilled into a small-sized sample of Φ =13 mm and x= 10 mm. Bosch Mini Hole Saw 5/8” HDG58 was used for core drilling [3].

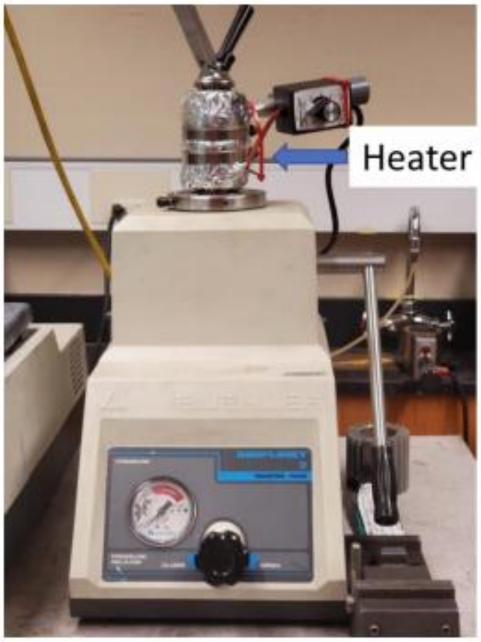

Figure 5: Beuhler mounting press [3]

Figure 6: Fischer scientific isotemp muffle furnace [3]

A scaled brake dynamometer was used to simulate the braking conditions. Bench-top tester shown in figure 7 was used for the testing. The testing was performed using non-asbestos organic pad samples and laboratory 3D-printed S316 stainless steel samples. The SAE J2522 Ak master procedure has 15 sections with section 4 having 5 sub-section, section 7, and section 12 having 2 sub-section each [12]. This first “burnishes” procedure consists of 64 burnish steps with the following other step to evaluate pressure, temperature, recovery, and speed on friction, wear, and noise propensity. In the speed pressure sensitivity section, the samples are tested at high-speed braking of up to 200 to 170 kph as well as at low-speed braking of 40 to 5 kph. The pressure sensitivity steps range from 80 to 30 kph and are tested at the pressure line range from 10 to 80 bars. Similarly, in the section obtaining the so-called characteristics values of pad friction performance, samples are tested on the high speed of

Normal force, frictional torque, rotational speed, and temperature are recorded during the test and recorded values are used for calculating brake effectiveness (μ) values. To simulate the heat developed during the braking phenomenon, an external heating chamber custom-built by BRUCKER was used as shown in Figure 7.

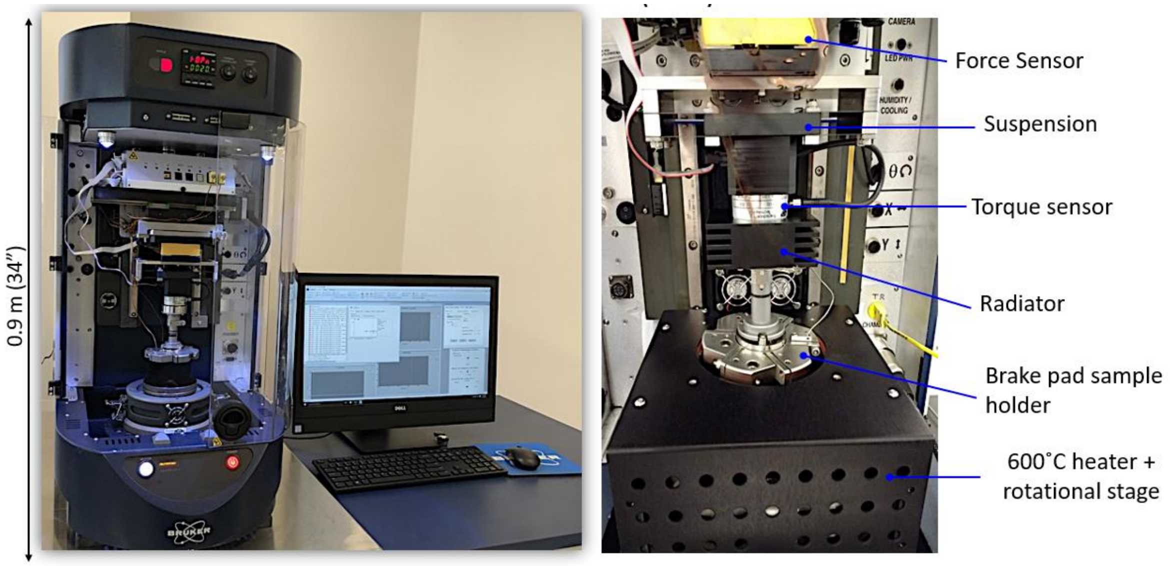

Figure 7: Bench-top tester (UMT) [3]

Bulk density and porosity for brake pads were analyzed using the Archimedes principle. The pad samples were suspended in a glass beaker filled with distilled water and were weighed using an analytical balance (AWS ALX – 310) for calculating bulk density. The following equations were used to calculate the bulk density of the brake pad sample [3]

$$Bulk\ Density\ = \frac{m}{v} = \frac{m1}{\frac{m1 - m2}{density\ of\ water}} = \frac{m1}{m1 - m2}$$

Where m1 is the dry mass (mass in the air), whereas m2 is the wet mass (mass while suspended in distilled water). Rockwell B hardness and Shore D hardness equipment is shown in Figure 8. They were used to measure the hardness of 3D printed stainless steel rotors and pad samples. The hardness was calculated before UMT testing for each of 3 rotor and pad samples.

(a) (b)

Figure 8: (a) Rockwell B hardness tester and (b) Shore D durometer

Once the friction testing is complete, the brake pad and rotor surface were analyzed using scanning electron microscopy (SEM), Quanta FEG 450 by FEI, and Energy Dispersive X-ray spectrometry (EDX, Oxford Instruments). Surface roughness after the friction test was also measured using pocket surf as shown in Figure 9. For the measurement of surface roughness, the probe of the instrument should be held on the surface of friction layer as shown in figure 9 and a button called R_a should be pressed. Pressing this button records the surface roughness for the surface where the probe was in touch with. The wear of the pad is calculated by weighing the mass of the pad and rotor samples using an analytical balance. The difference in the mass of samples before and after tests is used to calculate the value for the wear using the expression:

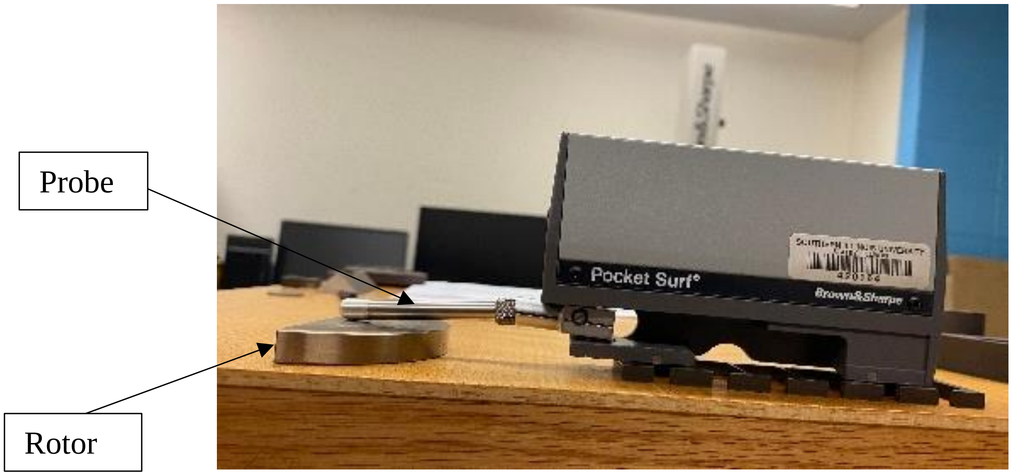

Figure 9: Pocket surf (Brown & Sharpe)

To study the microstructure and the grain size of the rotor sample, rotor samples were cut down into small pieces, polished and seen under polarized light microscope (PLM). First the cut down rotor piece is molded using EpoKwick FC, Epoxy resin which is hardened using an Epoxicure epoxy hardener. The resin and the hardener are mixed in the ratio of 3:1 and poured in a cup containing the cut down rotor sample as shown in figure 10. Then the poured resin in the cup is set for hardening for 24 hr. Once the resin with the cut down rotor sample as shown in figure 10 is hardened, they are fitted into a sample holder for polishing. These samples were polished using set of 180, 240, 320, 400, 600, 800, 1200, sized girt paper followed by final polishing with aluminum oxide slurry (Al203).

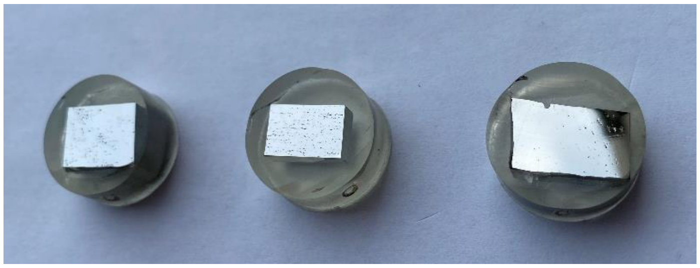

Figure 10: Polished rotor samples for PLM

CHAPTER 4

RESULTS AND DISCUSSION

This chapter details the friction performance of 3 SS316 rotor and laboratory manufactured pad samples, surface chemistry, and topography analysis using SEM (Scanning Electron Microscopy) and EDX (Energy Dispersive X-Ray) with a final discussion on the effectiveness of tested samples in electric vehicles (EVs). It also details the physical properties like hardness, porosity, bulk density, surface roughness of the 3 tested rotor samples followed by discussion of the results.

4.1 Friction test

The SAEJ2522 script was followed to simulate the actual braking phenomenon in UMT. It consists of 15 sections where the samples are tested in different ranges of temperatures, load, and speed. For burnishing, the cut-down samples are pressed against the rotor by applying 200 N force for 5 minutes with a relaxing time of 1 minute to prevent the samples from overheating. Burnish section improves the contact surface between pad and rotor which is important for the formation of good friction layer. However, while testing it should be ensured that there is at least 80% of contact area with the pad and brake rotor to get the effective result. The results were recorded by the control computer and MATLAB was used to generate plots. Plots generated against the coefficient of friction and pressure line; number of brake engagement are shown below for each of three samples.

Figure 11, 12, 13 details the average (Coefficient of Friction) COF values with different braking engagements for each 3 rotor samples. The blue lines in figure 11, 12, 13 represent the COF value at different brake engagements whereas the black dots are the average COF value at mentioned brake engagements. In µ green section for all 3 samples, COF value tend to increase with every brake engagement. Whereas in the bedding section for all 3 samples, COF values seems to be fluctuating with an average maximum COF value, 0.44, for sample 3. The friction coefficient was seen to be unstable and increasing in µ green section for all three samples with an average COF of 0.3 which is a very nice and high COF. Similarly, the COF fluctuates and keeps on increasing until the bedding and characteristics section for all three samples. The average COF of 0.42 and 0.45 was found in the bedding and characteristics section of the SAEJ2522 script. The number of brake engagements during µ green section was 1 to 30, 2 to 62 in bedding, and 1 to 6 in characteristics value. As shown in figure 11, 12, 13 until bedding section there is an increasing trend in COF and it stabilize during the characteristic value. This could be because of the formation of good surface contact between pad and rotor sample as proceeded into the SAE J2522 script. In µ green and bedding section brake rotor decelerates from 80 to 30 kph, and 40 to 5 kph in the section characteristics value.

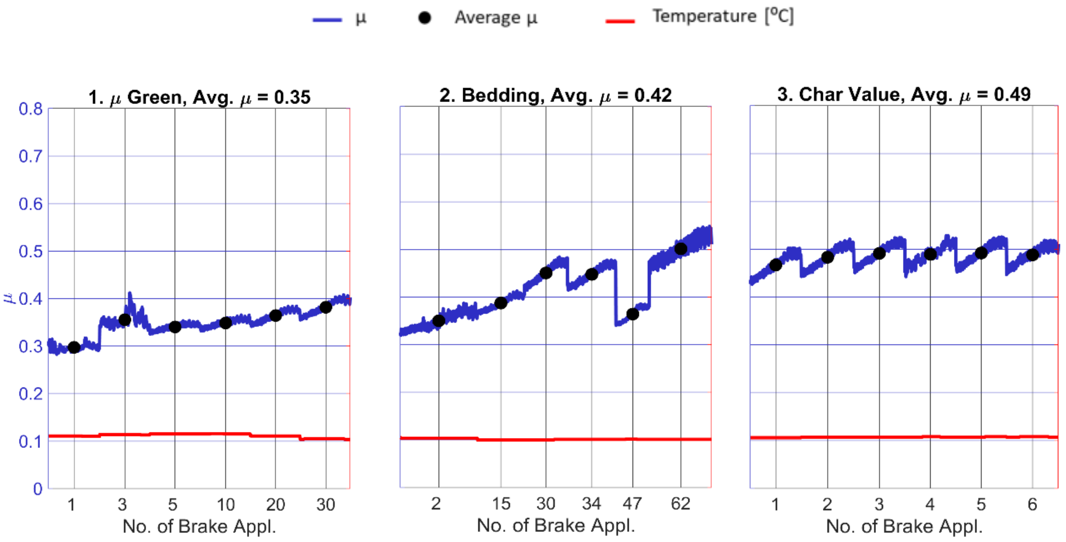

(a) (b) (c)

Figure 11: (a) µ Green, (b) Bedding, (c) Char value for sample 1

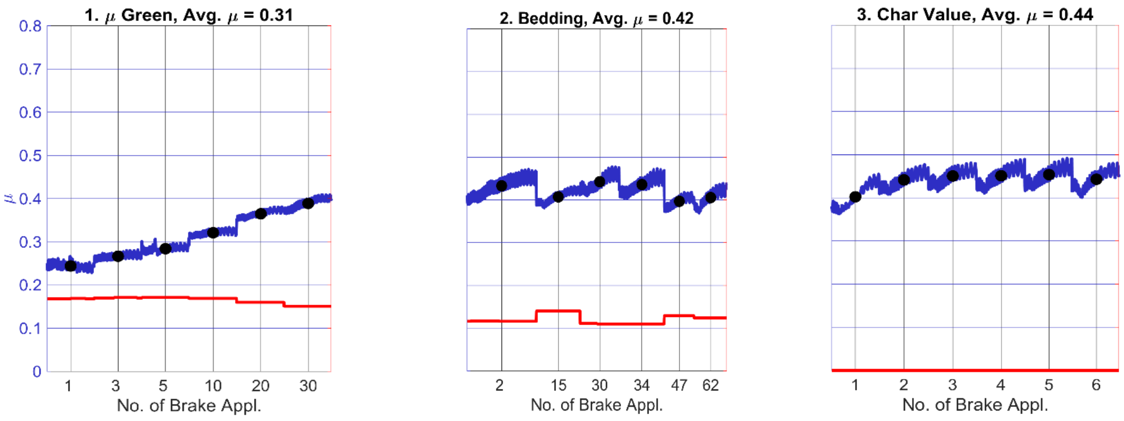

(a) (b) (c)

Figure 12: (a) μ Green (b) Bedding (c) Char value for sample 2

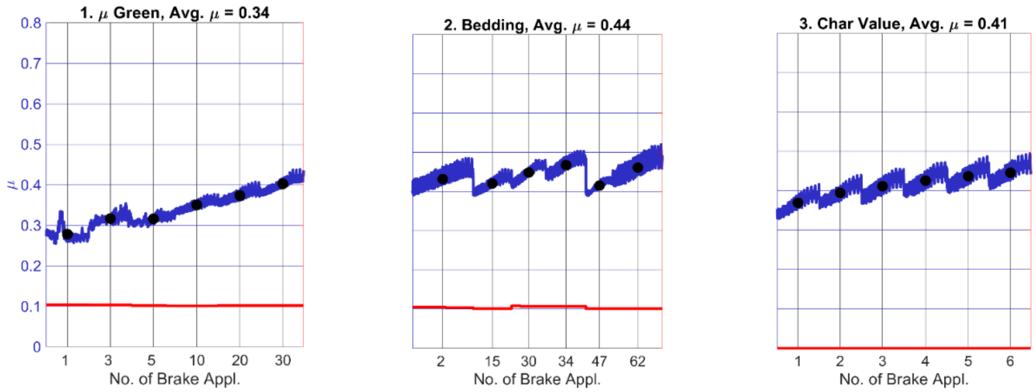

(a) (b) (c)

Figure 13:(a) μ Green (b) Bedding (c) Char value for sample 3

In the speed/pressure section, braking of rotating rotor and pad is achieved from high speed, 200 kph, and at high pressure up to 80 bars. This section helps to gauge the effectiveness of rotor/pad sample during emergency/ high speed braking. As shown in the figure 14, COF value is unstable and decreasing until 4.3 speed pressure sensitivity section. On further study of friction behavior of SS316 rotor with even more high speed/ pressure braking (section 4.4, 4.5), It was found that the unstable trend of COF gets stabilized by section 4.4, 4.5 with an average COF value of 0.37.

Also, during the cold application, the stainless-steel rotor acted well with an average COF of 0.4. The braking condition for the cold application is 80 to 30 kph whereas, in the case of high-speed braking, sections 4.1, 4.2, 4.3, 4.4, and 4.5, the braking speeds are 40 to 5 kph, 80 to 40 kph, 120 to 80 kph, 160 to 130 kph, 200 to 170 kph, respectively. This high and stable µ during braking will account for improved braking experience for user during high-speed braking. After high-speed braking, rotor and pad samples were tested for characteristic value and COF was found to be very stable and high after harsh braking condition which indicates that SS316 steel rotor was suitable for high speed/pressure braking.

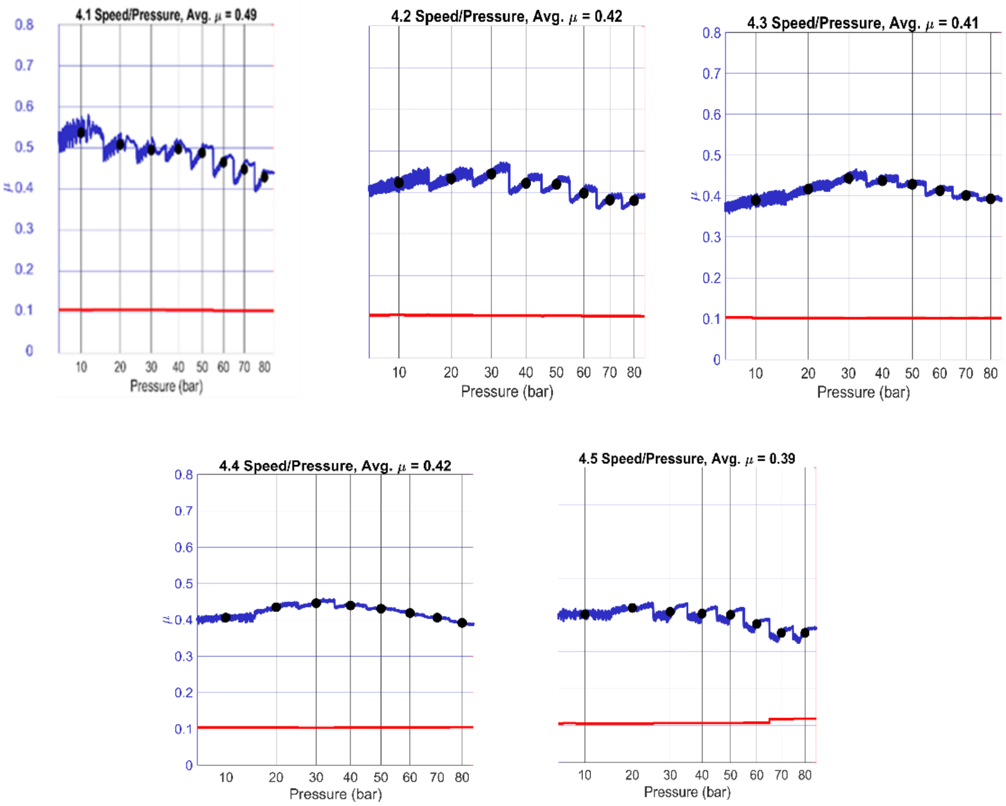

(a)

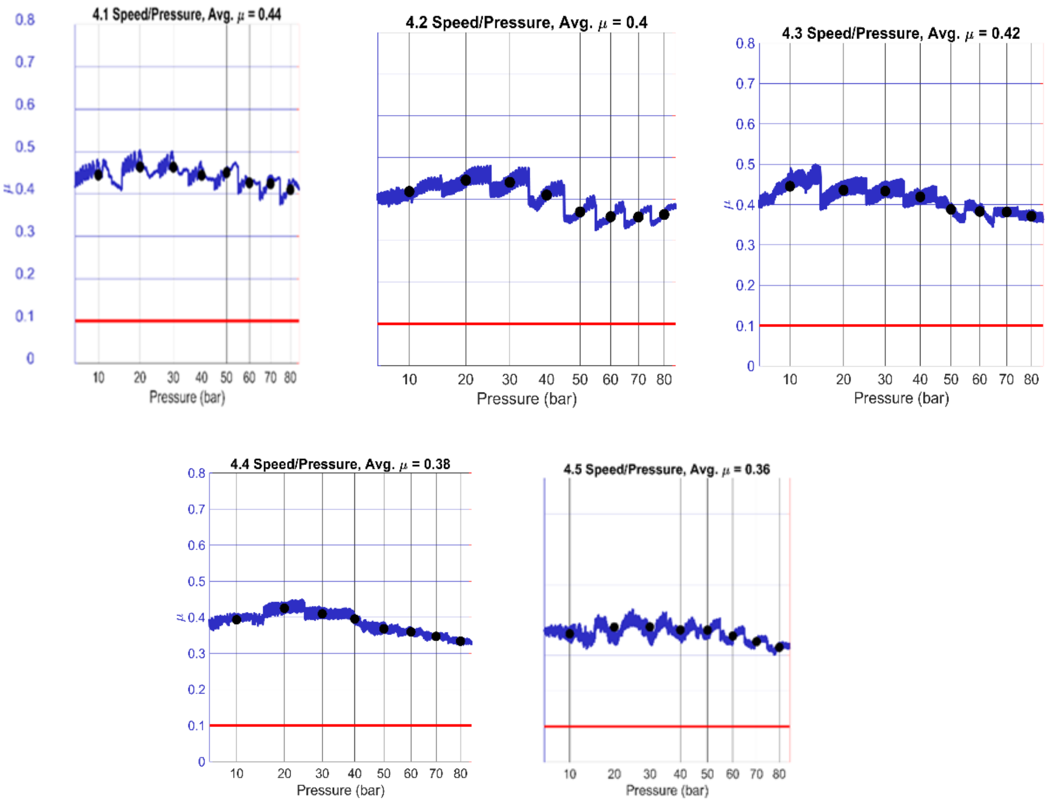
4.1 Speed/Pressure, Avg. μ = 0.44
4.2 Speed/Pressure, Avg. μ = 0.4
4.3 Speed/Pressure, Avg. μ = 0.42
4.4 Speed/Pressure, Avg. μ = 0.38
4.5 Speed/Pressure, Avg. μ = 0.36
μ
0 0.1 0.2 0.3 0.4 0.5 0.6 0.7 0.8
10 20 30 40 50 60 70 80
Pressure (bar)

(b)

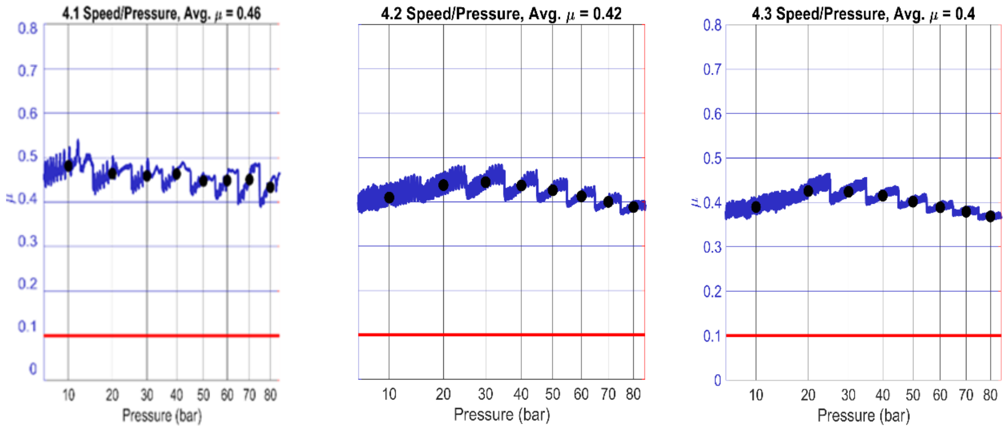
4.1 Speed/Pressure, Avg. μ = 0.46
4.2 Speed/Pressure, Avg. μ = 0.42
4.3 Speed/Pressure, Avg. μ = 0.4
μ
0 0.1 0.2 0.3 0.4 0.5 0.6 0.7 0.8
10 20 30 40 50 60 70 80
Pressure (bar)

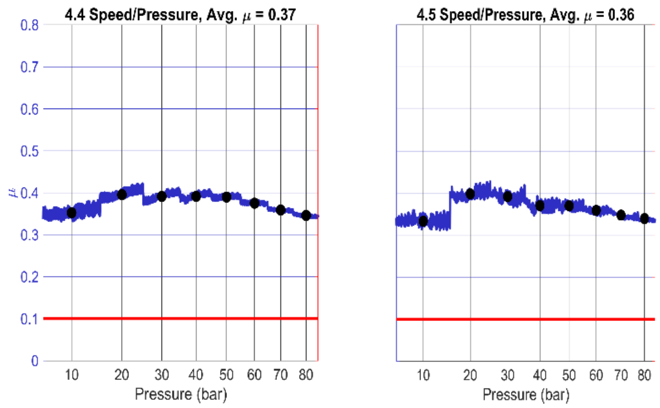

(c)

Figure 14: Friction testing -SAEJ2522 section 4.1, 4.2, 4.3, 4.4, 4.5 (a) sample 1, (b) sample 2, (c) sample 3

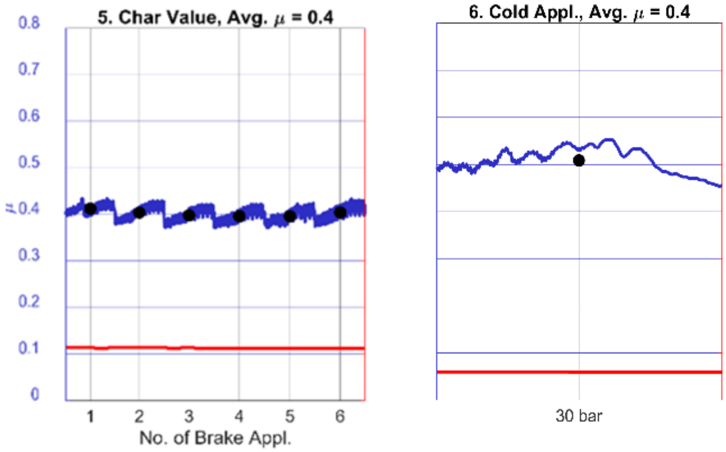

(a)

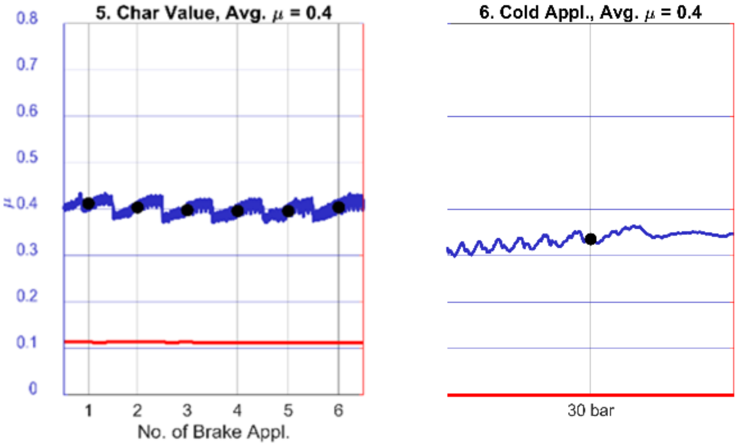

(b)

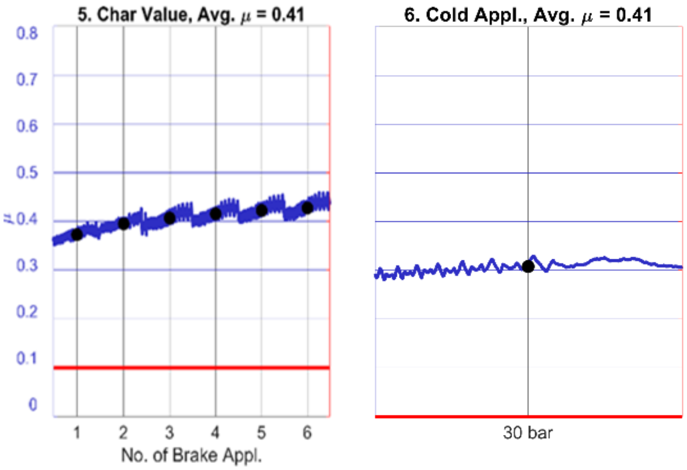

(c)

Figure 15: Friction testing-SAEJ2522 section 5, 6, (a) Sample1, (b) Sample 2, (c) Sample 3

The COF in motorway snubs sections is found to be very stable with an average μ of 4.1 for both samples 2 and 3. As shown in figure 16, Sections 7.1 and 7.2, the COF increases as we go toward the right side of the graph, and it continues increasing until section 12, the characteristic value, with an average μ of 0.46. Whereas in fade 1, the temperature is comparatively high compared to other sections of SAEJ2522 and hence results in low and very unstable COF with an average μ value of 0.3 for samples 2 and 3. This drop in COF in high temperature testing could be because of low thermal conductivity of SS316 rotor.

Similarly, a very stable COF is found in all other sections of characteristics value, pressure line, and fade 2. The maximum average COF among char values is found in section 8 with an average μ value of 0.46 which is very high and in the pressure line section, the average μ value of 0.3 is found for samples 2 and 3. Lastly, in fade 2, the COF is found to be very stable with an average COF of 0.3. This indicates that SS316 rotor provides smooth braking experience during high temperature braking.

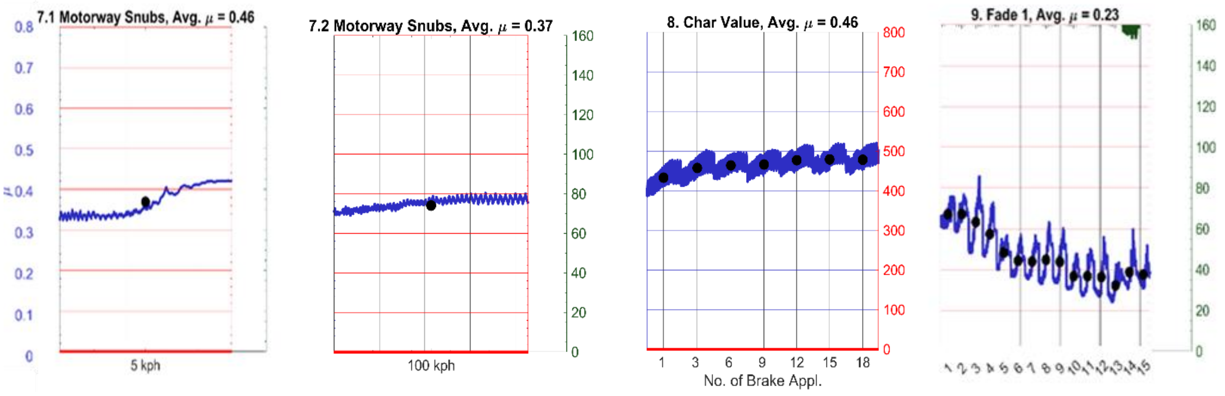
7.1 Motorway Snubs, Avg. μ = 0.46
μ
0.8
0.7
0.6
0.5
0.4
0.3
0.2
0.1
0
5 kph
7.2 Motorway Snubs, Avg. μ = 0.37
100 kph
160
140
120
100
80
60
40
20
0
8. Char Value, Avg. μ = 0.46
800
700
600
500
400
300
200
100
0
1 3 6 9 12 15 18
No. of Brake Appl.
9. Fade 1, Avg. μ = 0.23
1 2 3 4 5 6 7 8 9 10 11 12 13 14 15
160
140
120
100
80
60
40
20
0

(a)

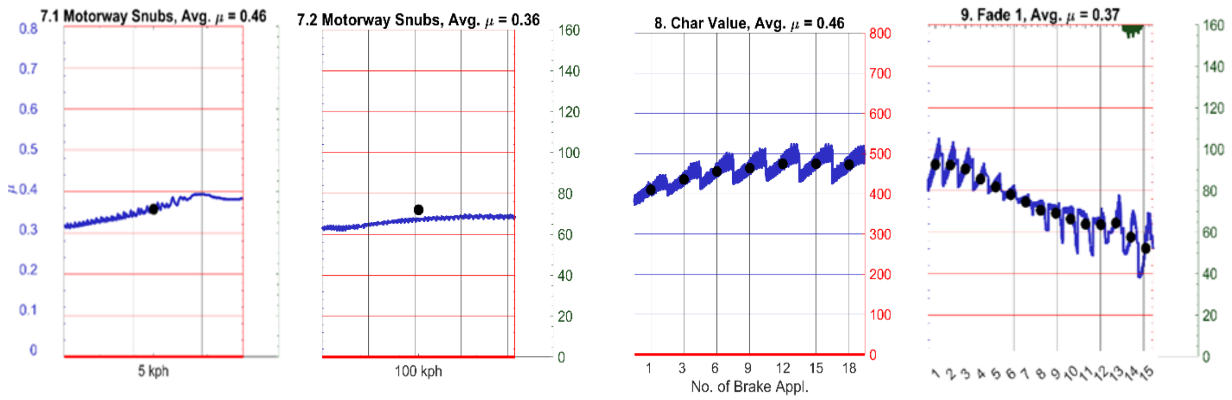
7.1 Motorway Snubs, Avg. μ = 0.46
μ
0.8
0.7
0.6
0.5
0.4
0.3
0.2
0.1
0
5 kph
7.2 Motorway Snubs, Avg. μ = 0.36
100 kph
160
140
120
100
80
60
40
20
0
8. Char Value, Avg. μ = 0.46
800
700
600
500
400
300
200
100
0
1 3 6 9 12 15 18
No. of Brake Appl.
9. Fade 1, Avg. μ = 0.37
1 2 3 4 5 6 7 8 9 10 11 12 13 14 15
160
140
120
100
80
60
40
20
0

(b)

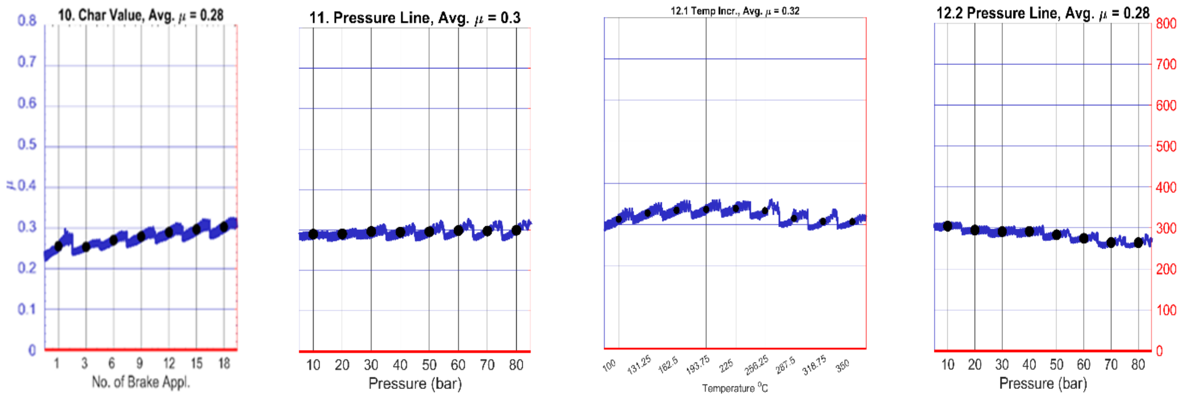
10. Char Value, Avg. μ = 0.28
μ
0.8
0.7
0.6
0.5
0.4
0.3
0.2
0.1
0
1 3 6 9 12 15 18
No. of Brake Appl.
11. Pressure Line, Avg. μ = 0.3
10 20 30 40 50 60 70 80
Pressure (bar)
12.1 Temp Incr., Avg. μ = 0.32
100 131.25 162.5 193.75 225 256.25 287.5 318.75 350
Temperature °C
12.2 Pressure Line, Avg. μ = 0.28
10 20 30 40 50 60 70 80
Pressure (bar)
800
700
600
500
400
300
200
100
0

(a)

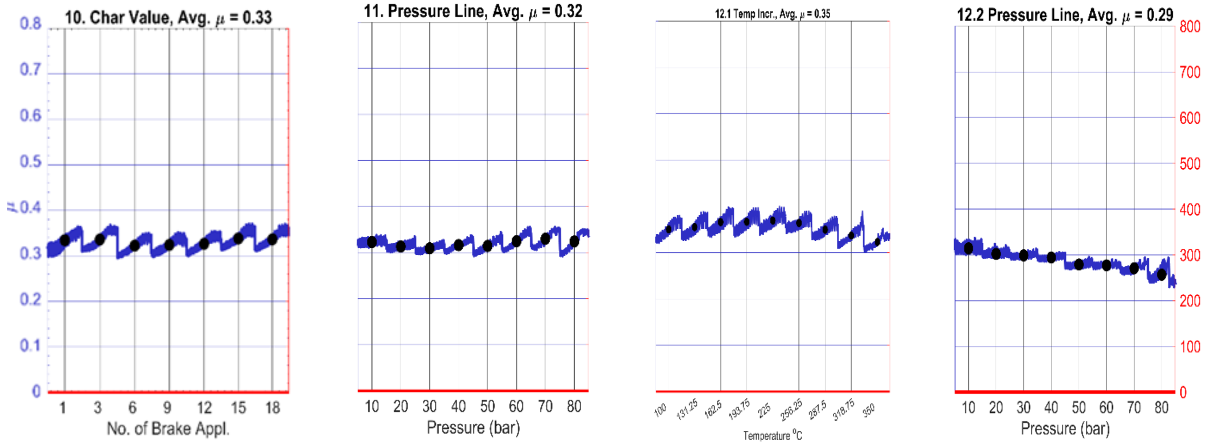
10. Char Value, Avg. μ = 0.33
μ
0.8
0.7
0.6
0.5
0.4
0.3
0.2
0.1
0
1
3
6
9
12
15
18
No. of Brake Appl.
11. Pressure Line, Avg. μ = 0.32
10
20
30
40
50
60
70
80
Pressure (bar)
12.1 Temp Incr., Avg. μ = 0.35
100
131.25
162.5
193.75
225
256.25
287.5
318.75
350
Temperature °C
12.2 Pressure Line, Avg. μ = 0.29
800
700
600
500
400
300
200
100
0
10
20
30
40
50
60
70
80
Pressure (bar)

(b)

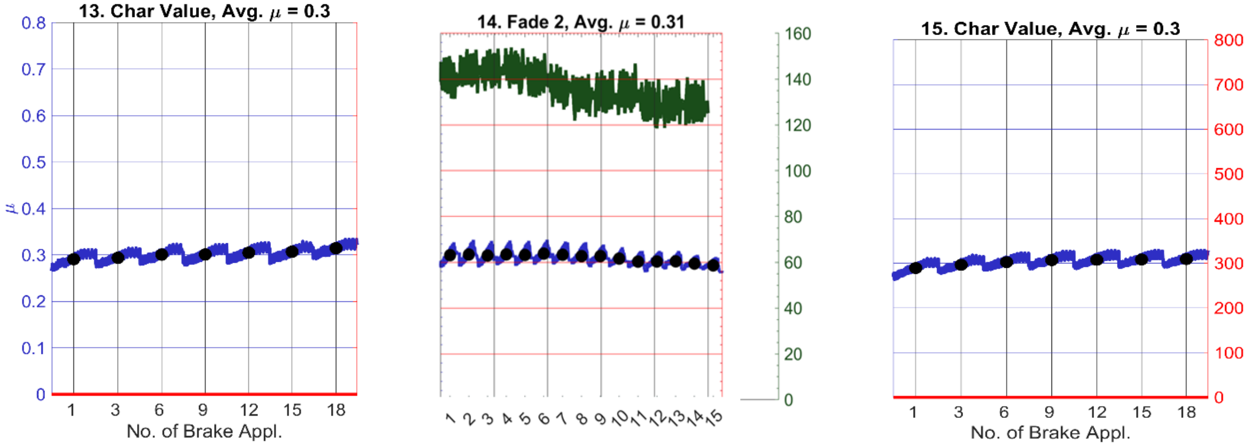
13. Char Value, Avg. μ = 0.3
μ
0.8
0.7
0.6
0.5
0.4
0.3
0.2
0.1
0
1
3
6
9
12
15
18
No. of Brake Appl.
14. Fade 2, Avg. μ = 0.31
160
140
120
100
80
60
40
20
0
1
2
3
4
5
6
7
8
9
10
11
12
13
14
15
15. Char Value, Avg. μ = 0.3
800
700
600
500
400
300
200
100
0
1
3
6
9
12
15
18
No. of Brake Appl.

(a)

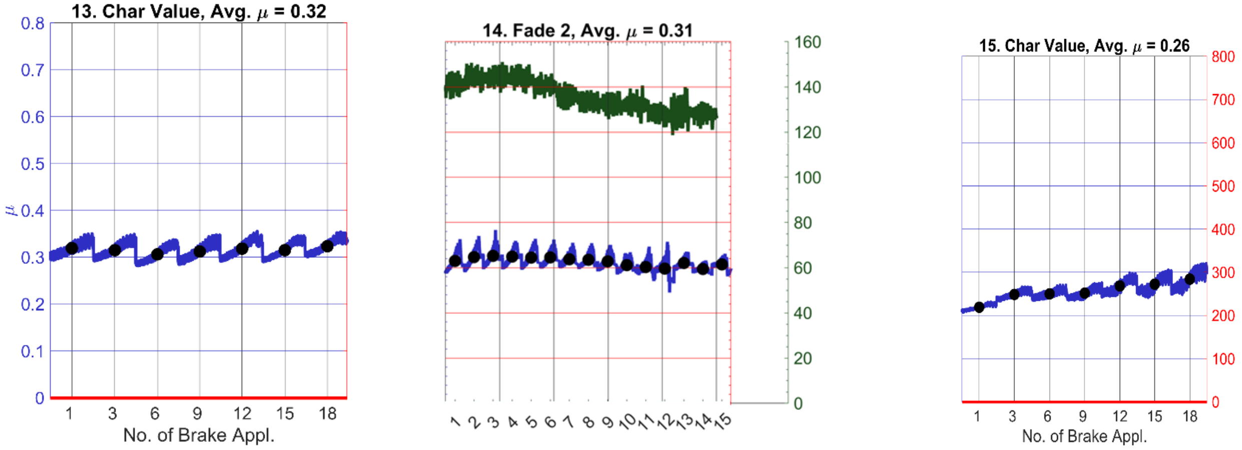
13. Char Value, Avg. μ = 0.32
μ
0.8
0.7
0.6
0.5
0.4
0.3
0.2
0.1
0
1
3
6
9
12
15
18
No. of Brake Appl.
14. Fade 2, Avg. μ = 0.31
160
140
120
100
80
60
40
20
0
1
2
3
4
5
6
7
8
9
10
11
12
13
14
15
15. Char Value, Avg. μ = 0.26
800
700
600
500
400
300
200
100
0
1
3
6
9
12
15
18
No. of Brake Appl.

(b)

Figure 16: Friction testing- SAEJ2522 Section: 7.1, 7.2, 8, 9, 10, 11, 11.1, 11.2, 12, 13, 14, 15 (a) sample 2, (b) sample 3

Figure 17 shows the three-3D printed stainless steel rotor sample and laboratory manufactured NAO brake pads. The surface of rotor and pad are grinded using 180 size grit paper so that they have same surface roughness before the UMT friction test.

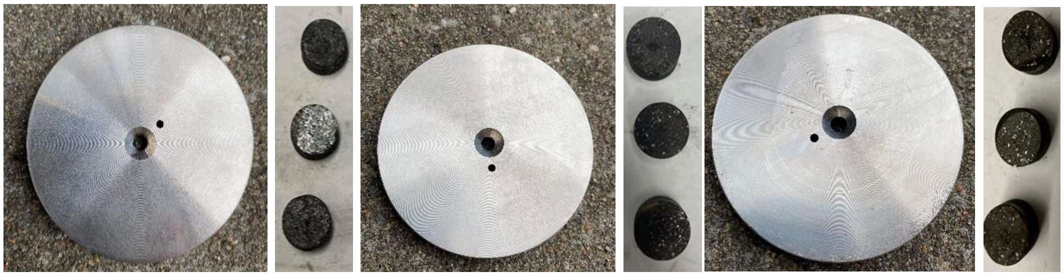

Figure 17: 3D printed SS316 rotor and laboratory-formulated NAO pad samples.

As shown in Figure 17 the maximum average μ value was seen in sample 1 at the section 4 of speed pressure sensitivity. While performing UMT test for sample 1, the objective was to look for the effectiveness/COF of SS316 rotor when braking from high speed and pressure. Hence for sample 1, UMT test was only performed until speed pressure sensitivity section. However, sample 2, and 3 were tested for full SAEJ2522 sections and it was evident from the figure that sample 3 results in more stable and higher average COF compared to sample 2 in terms of COF and friction behavior.

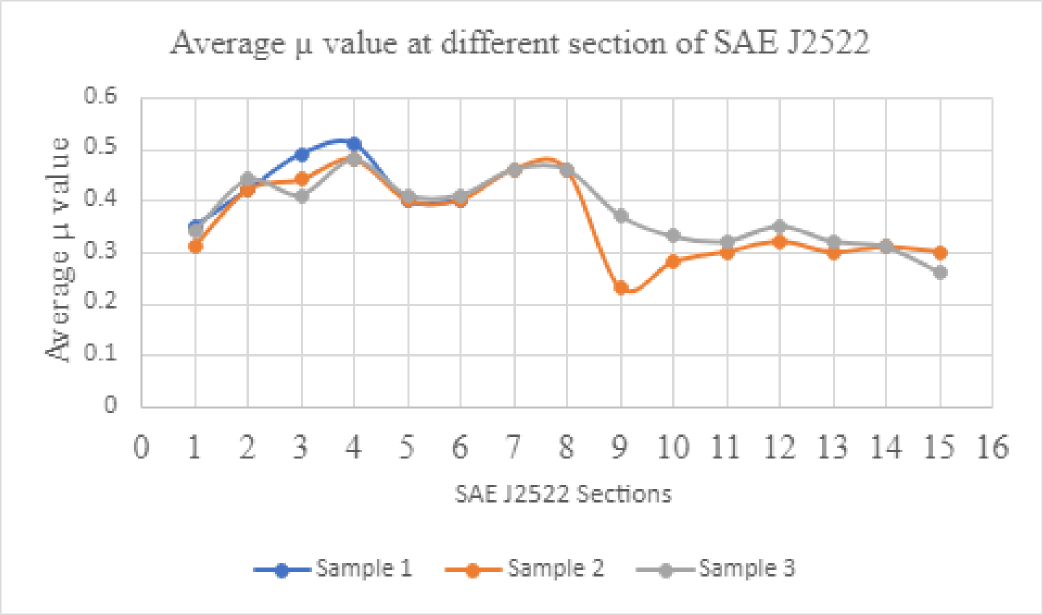

Figure 18:Average µ value at a different section of SAE J2522

Figure 19 shows the surface of 3D printed rotor and laboratory manufactured pad samples after UMT test. The rotor sample 2, 3 turns yellow because of testing at high temperature up to 350 °C during fade section. The circular groves in rotor as shown in figure 19 are the friction layer developed after friction test. Also, the shining grooves are seen on the pad surface representing the friction layer developed in pad.

Figure 19: 3D printed SS316 rotor and laboratory-formulated NAO pad samples

Wear in terms of thickness loss and mass loss is shown in figure 20. The maximum wear (0.45 g) is seen in rotor sample 1 and the minimum wear (0.12 g) is seen in rotor sample 2. These results can be correlated with the hardness of the respective rotor samples. As rotor 2 has a high hardness value compared to rotors 1 and 3, it results in low wear compared with the other 2 rotors. However, maximum thickness loss (0.045mm) is seen for sample 3, not for sample 1(0.01 mm). Similarly, wear in pad samples after the fiction test was compared and the maximum wear is seen for pad sample 2 with mass and thickness loss of 0.59 g and 2.87 mm respectively whereas the minimum wear is seen for pad sample 1. As seen in figure 20, there is discrepancies on mass and thickness loss of rotor and pad samples. Maximum mass loss, 0.45 g, was seen for rotor 1, whereas maximum thickness loss, 0.02 mm, was seen for rotor sample 2. Similarly, pad sample 3 wears most in terms of mass, however pad sample 2 wears most in terms of thickness.

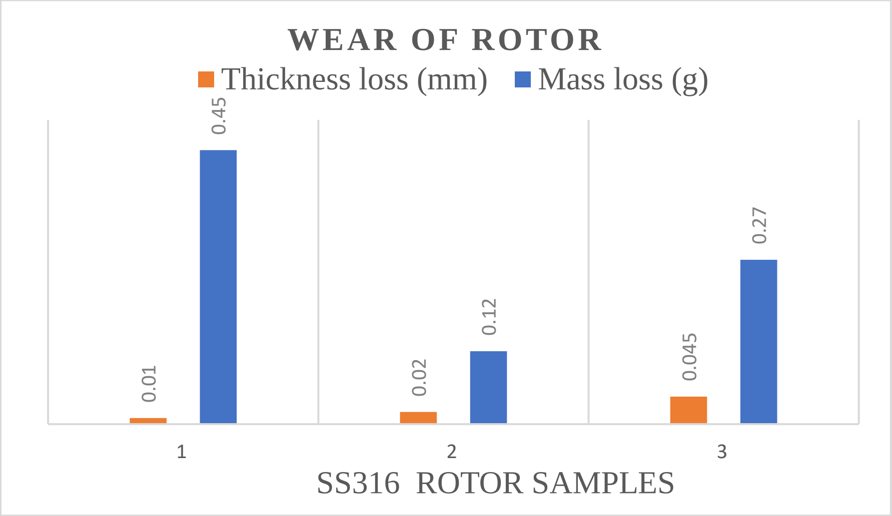

(a)

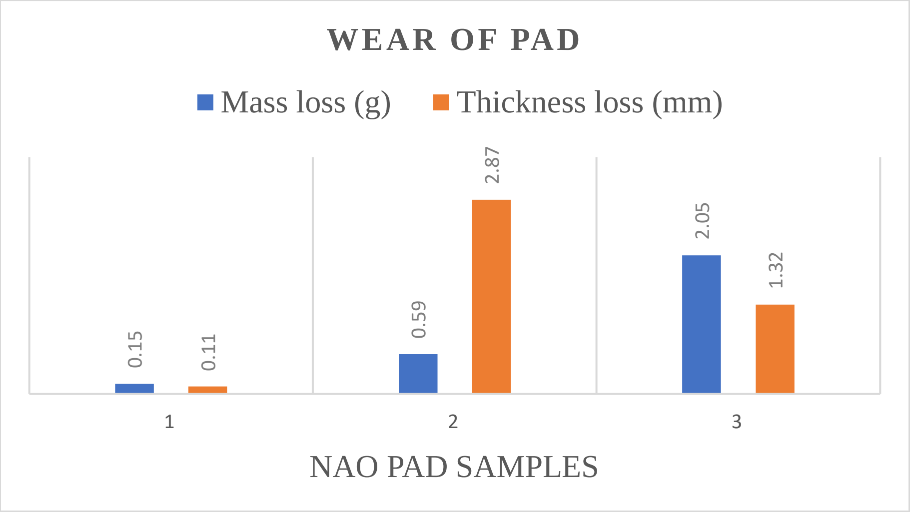

(b)

Figure 20: Wear of (a) rotor (b) pad samples

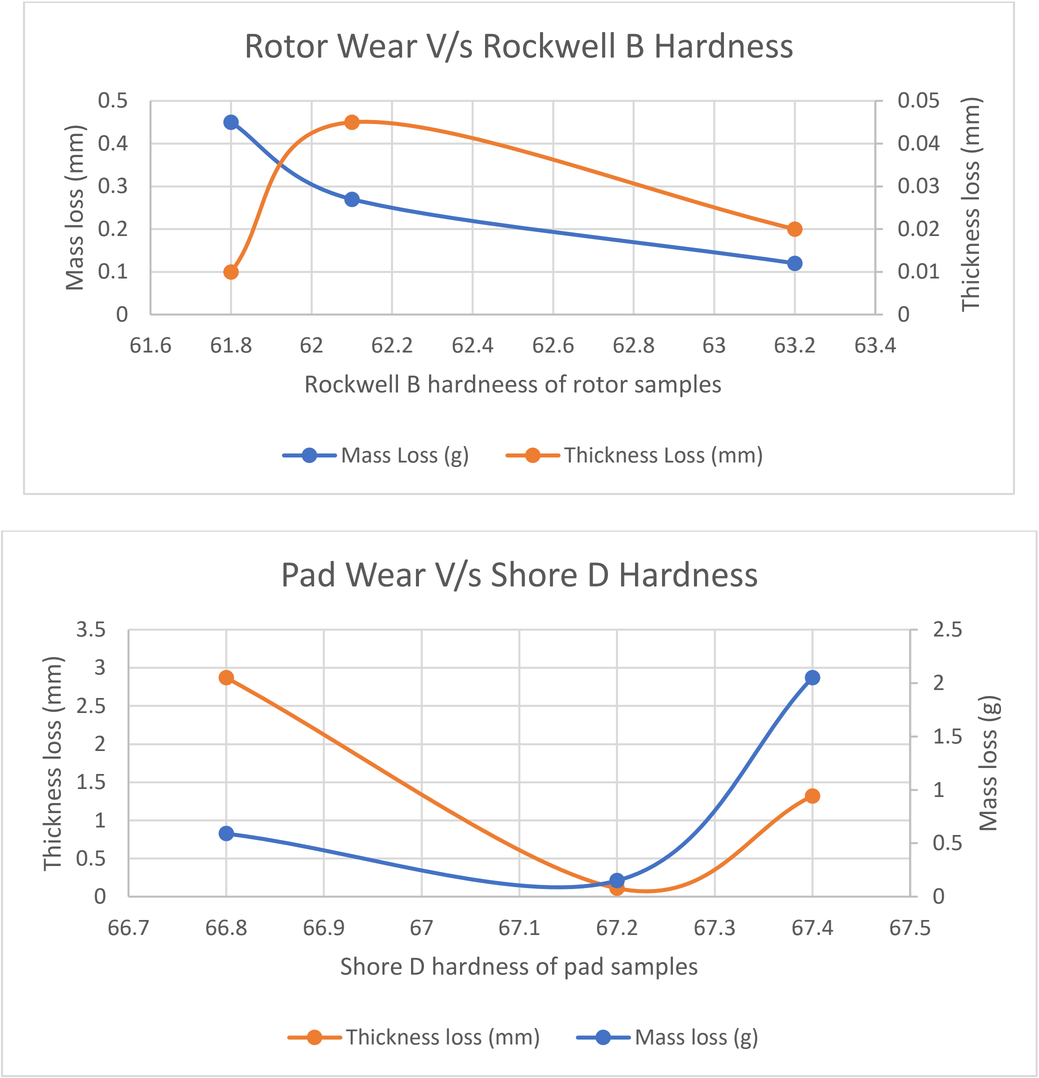

Figure 21: Wear Vs. hardness of rotor and pad samples

4.2 Physical properties of samples

To understand the science behind the difference in the COF value with 3 different 3D-printed rotor samples, its physical properties were explored. Since the SS rotors were 3D printed in the lab, they are highly porous compared to the cast iron rotor. Figure 22 details the bulk density, porosity, hardness, and surface roughness of the rotor which may be responsible for difference in the COF value for 3 SS316 rotor sample. Sample 3 has the highest bulk density, and it could be because of the differences in direction of 3-D printing of each layer. As bulk density increases, the space for porosity decreases. As sample 3 has the highest bulk density, it is least porous rotor sample. However, sample 2 has the lowest bulk density, but it is not the most porous rotor sample. Sample 1 is the rotor with maximum porosity of 2.17 %. Although all 3 rotors are made of the same material and have equal dimensions, they have different porosity. As these rotor samples were 3-D printed, the difference in the printing direction could account for difference in the porosity. To avoid the different starting condition of friction test, both rotor and pad sample surface are made similar, equal surface roughness, using 180 size grit paper. Hence, the surface roughness before test does not play any significant role in determining the friction behavior of tested rotor samples.

The average COF of three different SS316 rotors can be correlated with their porosity and surface hardness. As shown in figure 22, sample 2 (1.377 %) is more porous than sample 3 (0.047 %) and it has the lowest COF value, 2.3, at section 9 (Fade 1). Hence, it seems that highly porous material results in low COF compared to the one with low porosity. A similar result was found in a study conducted by Li, and Olofsson et al [38] where they found a decrease in friction coefficients as an increase in pore size in powder metallurgical gear materials. Similarly, Figures 18 and 22 showed that sample 2 having the highest surface hardness, 63.2 HRB, has the lowest COF. Moreover, rotor samples are tested at high temperatures in the pressure line, and the fade section of SAE J2522 was found to have a lower COF compared to other sections. Since these samples are subjected to high temperatures, their surface gets heat hardened resulting in lower COF values as shown in figure 17. In a study conducted by Devaraju et al. [[39] it was found that due to an increase in resistance to adhesion in harder material, there is a reduction in the friction characteristics of metals resulting in lower COF values. As shown in figure 22, the surface roughness of friction layer is high for rotor 2 compared to rotor 1, and 3. The wear in rotors 2 and 3 are comparable, However the pad sample 2 wears more compared to pad sample 3. This indicates that rotor and pad sample 2 wears the most.

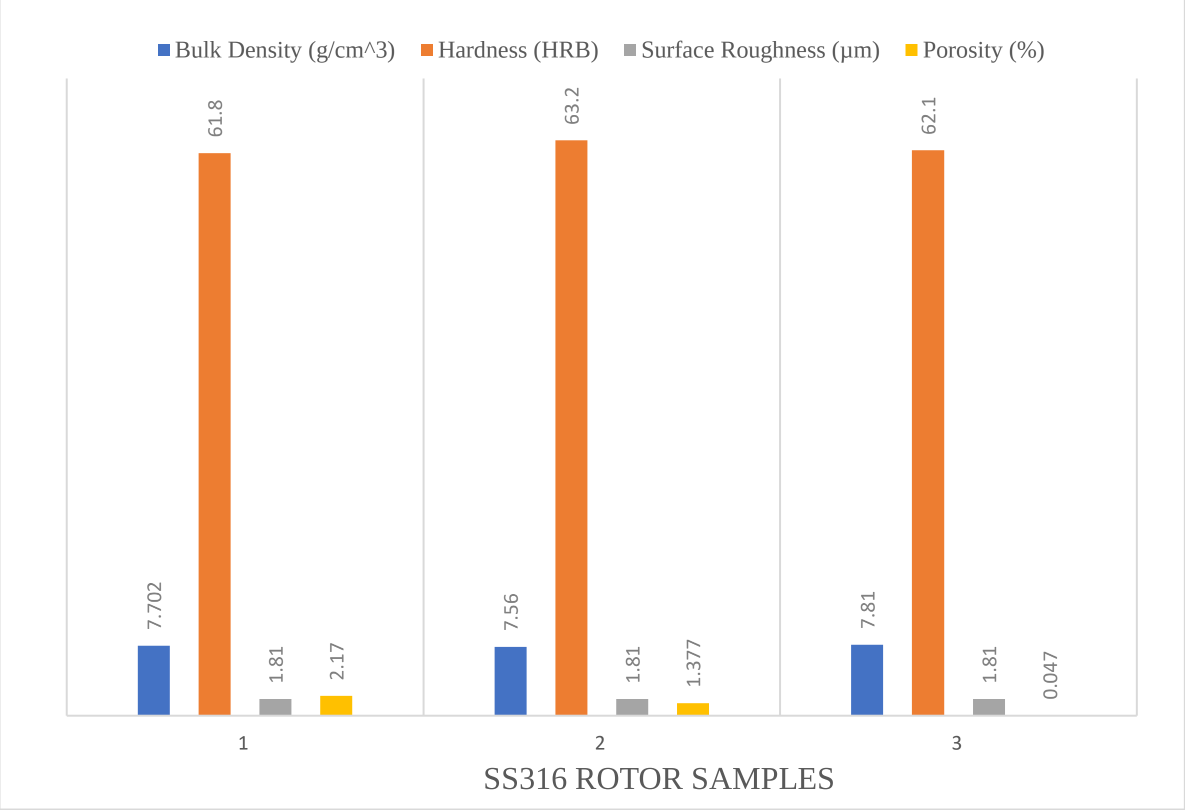

Figure 22: Physical properties of 3 SS316 rotor samples

4.3 SEM and EDX results

Moreover, to better understand the difference in the COF and wear, each rotor and pad sample were analyzed using SEM and EDX. Figure 23 shows the SEM of the friction surface of the 3 rotor samples. A continuous and very well-formed friction layer is found in rotor sample 1 and 3. As shown on figure 23, rotor sample 1 and 3 have adhesive friction layer, However, rotor sample 2 have combination of abrasive and adhesive friction mechanism. Although rotor 2 and 3 have comparable wear rate, pad sample 2 wear most compared to pad sample 3. This indicates that development of abrasive friction mechanism results on higher wear rate than adhesive friction mechanism.

Almost all surface of rotor 3 is covered with a continuous friction layer. This could be contributing to the high and stable COF value. A combination of abrasive and adhesive mechanisms is seen in the rotor sample 2.

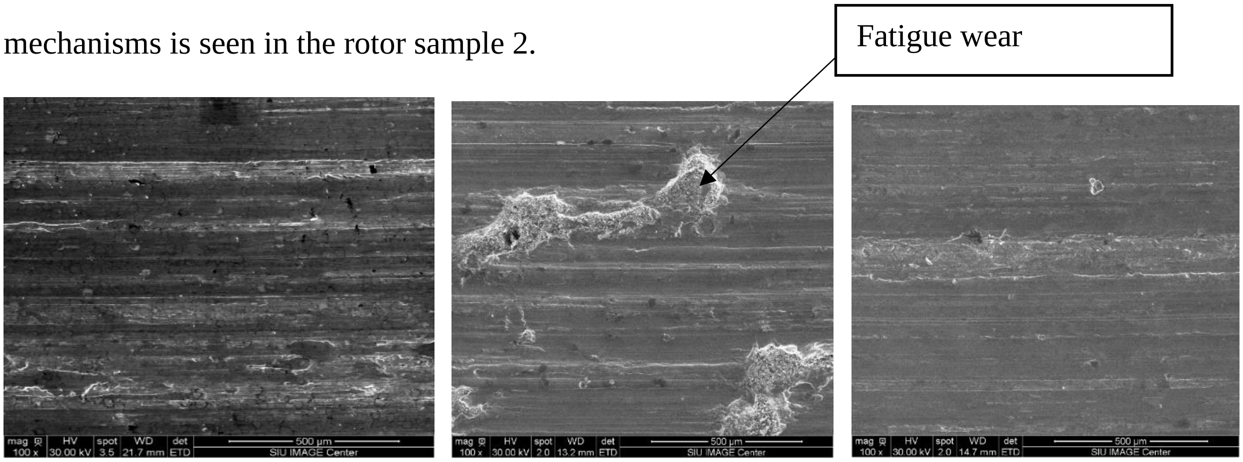

(a) (b) (c)

Figure 23: SEM microscopy result of tested rotor samples, (a) sample 1 (b) sample 2 (c) sample 3

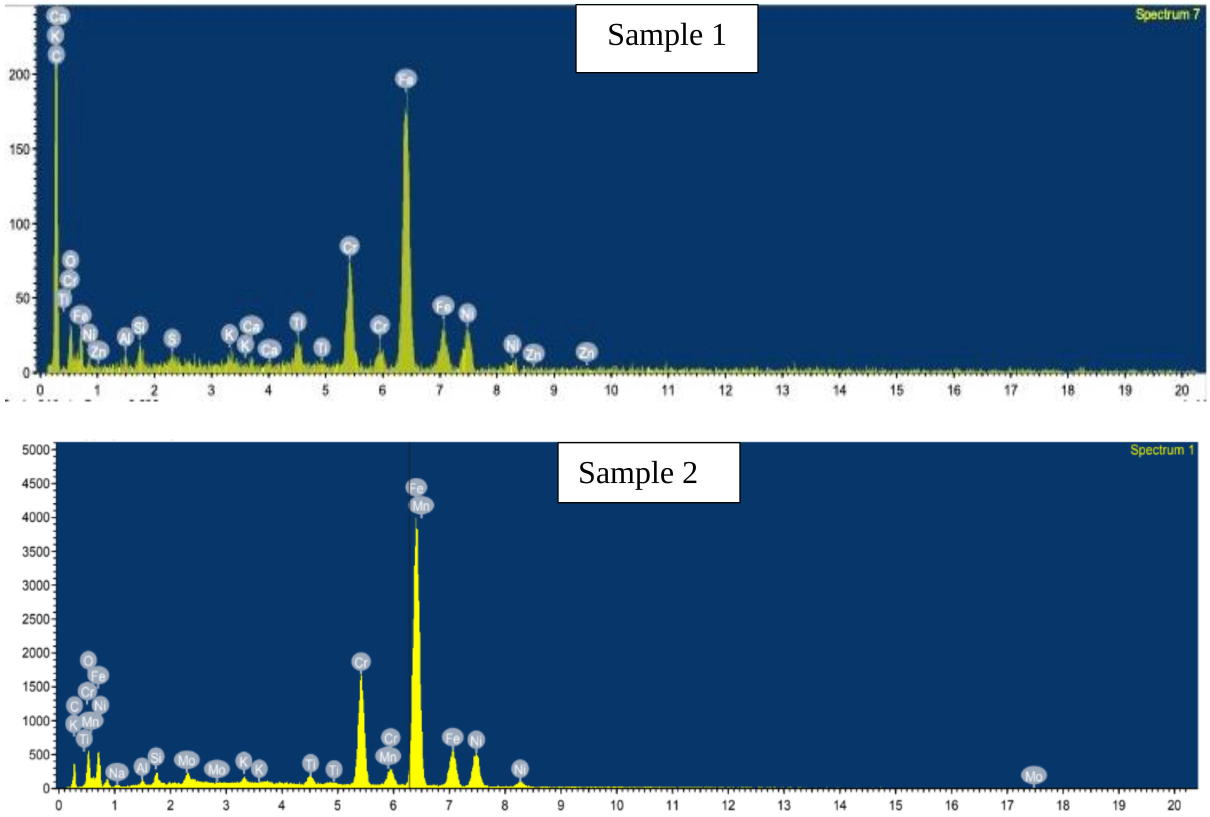

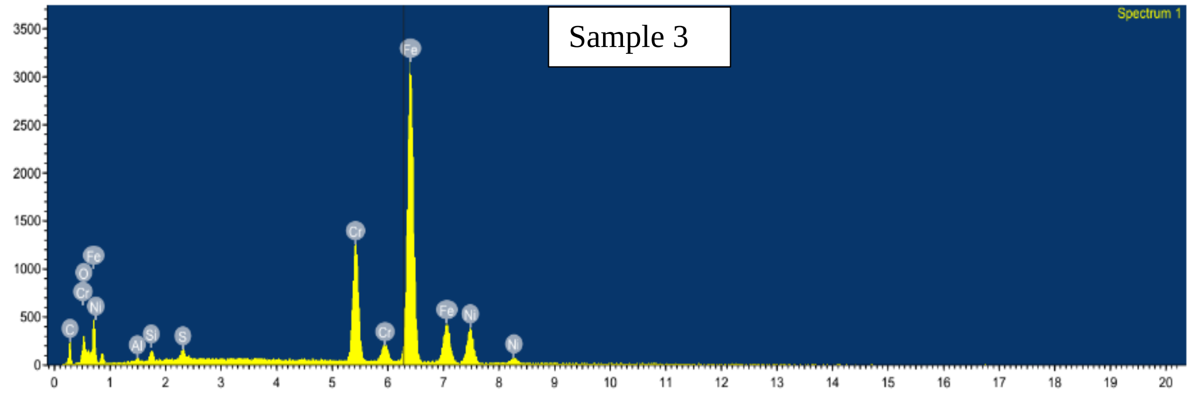

Figure 24: Rotor surface chemistry after friction test

Figure 24 shows the chemistry of the friction layer of the rotor. The presence of Ca, Si, Al, Zn, and K on the SS316 rotor shows that there is some material transfer from the pad to the rotor during the friction test. This could be the reason for the mass gain in rotor samples.

SEM of pad samples before and after the friction test shown in Figures 25 and 26 shows the surface of the pad sample before and after test respectively. There is the development of the good friction layer on pad sample 1, However, friction layer is not well developed on pad surface 2 and 3. There is transfer of bulk element on the surface of pad sample after friction test. Figure 25 and 26 shows the presence of carbonaceous material, glass fibers transferred on the surface of friction layer. The graphitic and other carbonaceous material layer is covered well by the developed friction layer on sample 1 as shown in figure 26. The shining component in Figure 2 is metallic components which are partially covered by the friction layer developed in the surface of pad sample 1.

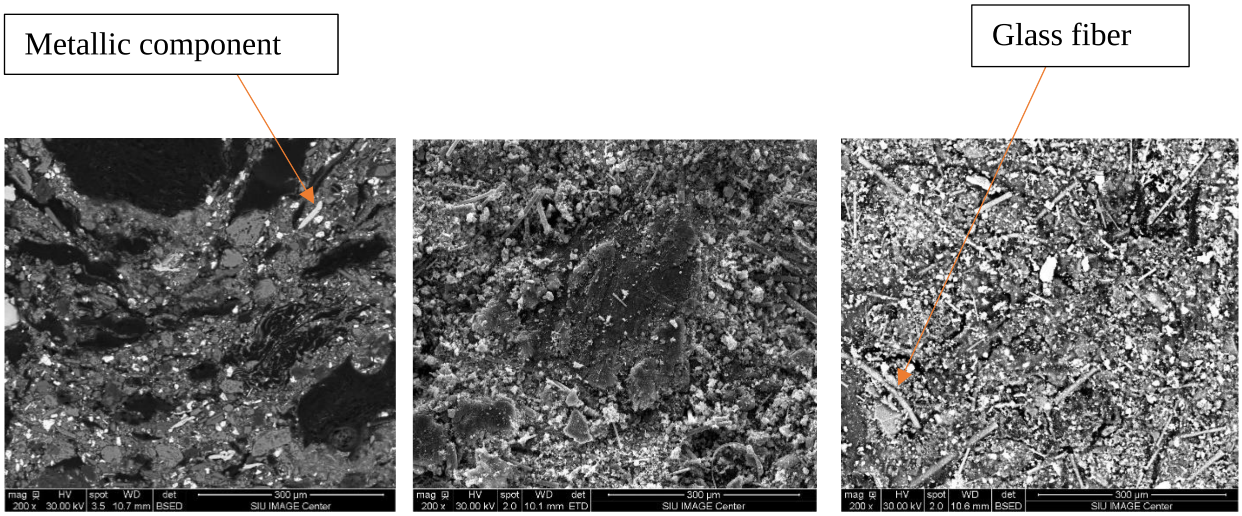

(a) (b) (c)

Figure 25: Pad surface before friction test, (a) sample 1 (b) sample 2 (c) sample 3

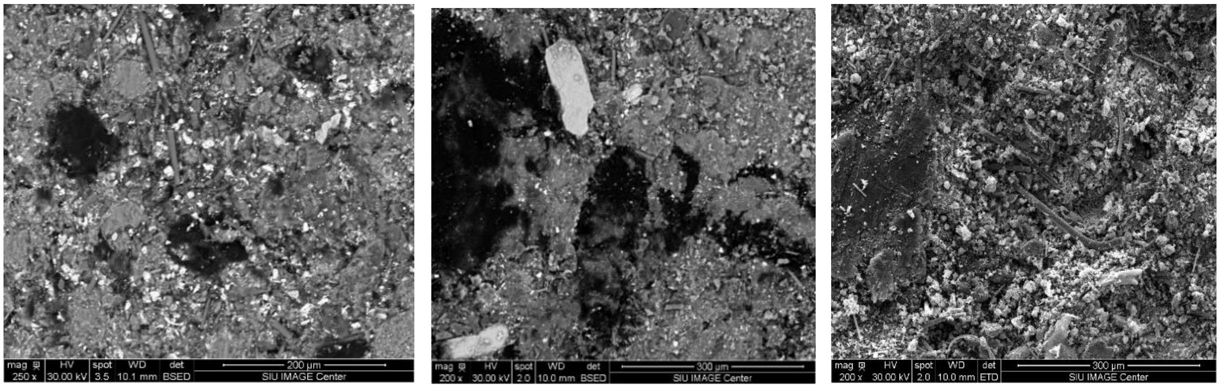

(a) (b) (c)

Figure 26: Pad surface after friction test, (a) sample 1 (b) sample 2 (c) sample 3

The yellow dependence in figure 27 shows the percentage of elements in pad surface before test whereas red dependance represents the percentage of element in pad surface after friction test. Surface chemistry of the pad surface is like bulk chemistry. As shown in figure 27, 28, and 29, more elements from bulk layer get transferred to the surface layer of pad samples after test. The quantity of elements like Ca, K, Ti, Si, Al increases on the surface of pad after friction test as they were transferred from the bulk surface. There is no significant material transfer from the rotor to the pad surface as the rotor elements like Fe, Cr, Ni are rarely seen in the EDX image of the pad samples.

Figures 28 and 29 shows the pad surface chemistry for sample 2 and 3. Si, Ca, K, Ti, Cr, and Al are present in bulk in the pad surfaces. The presence of elements like Al, Si, O, S on the friction surface alters the adhesion and friction behavior for stainless steel alloy. Comparing EDX result shown in figure 27 and 28, rotor sample 2 have higher amount of O in the friction surface compared to rotor sample 3. This could be responsible for low adhesion and friction behavior of rotor 2. In a study conducted by Devaraja et al. found that segregation of aluminum on the copper surface increases adhesion and friction however, segregation of element with small atomic radius like S, P, O, Si decrease the adhesion and friction level [39]

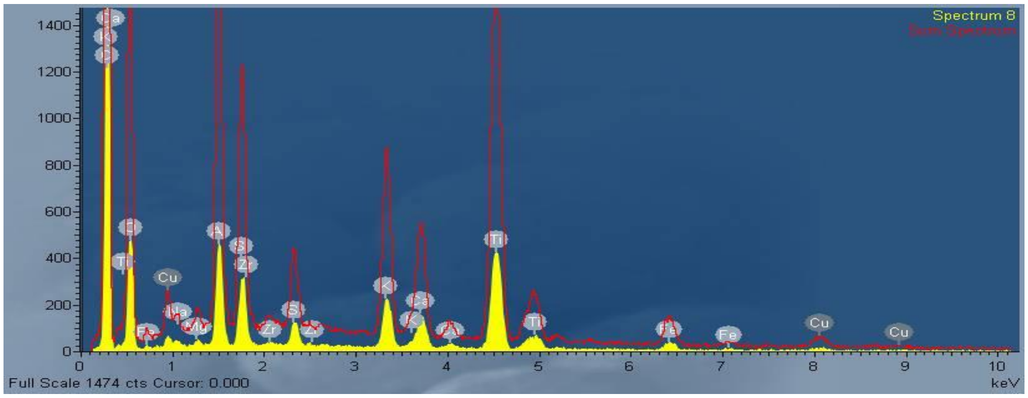

Figure 27: Pad surface chemistry before and after test for sample 1

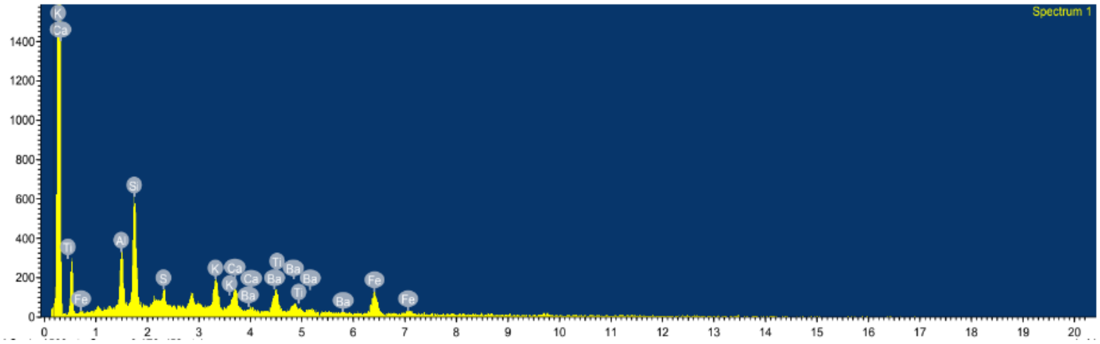

(a)

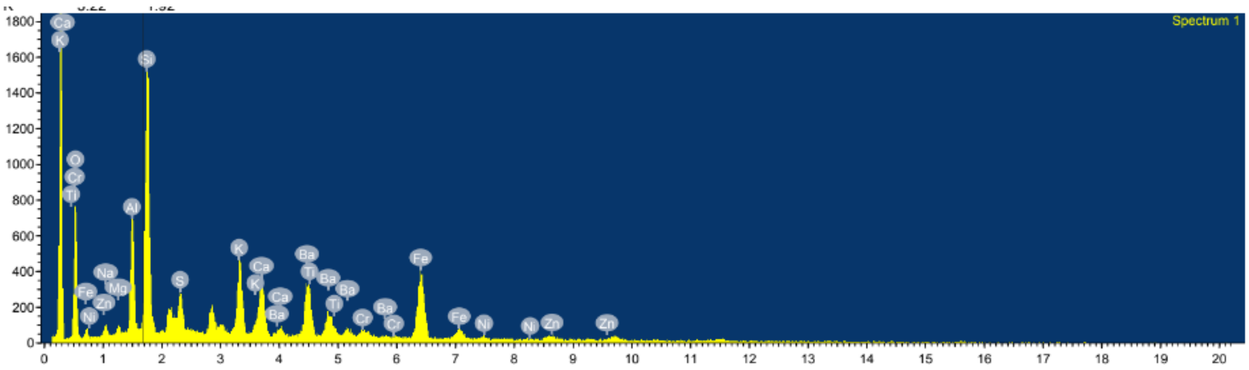

(b)

Figure 28: Pad surface chemistry of sample 2 (a) before (b) after friction test

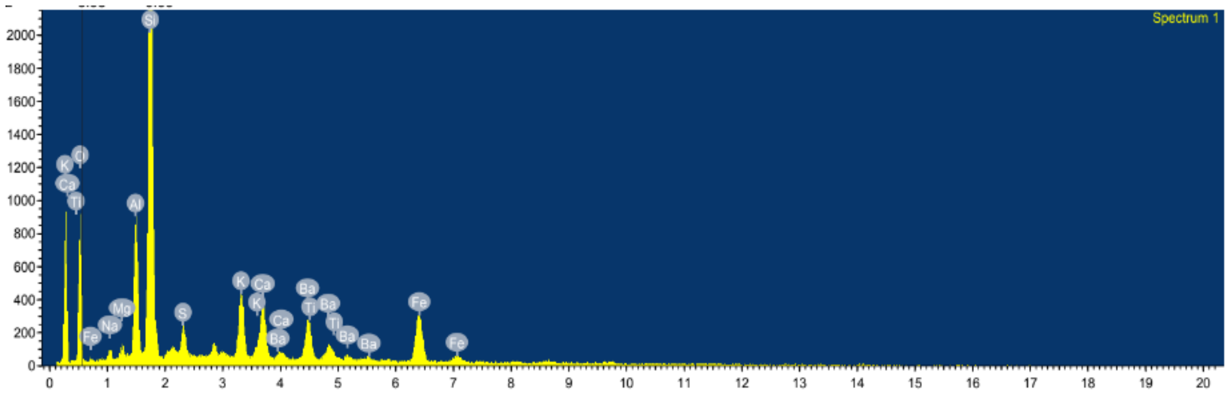

(a)

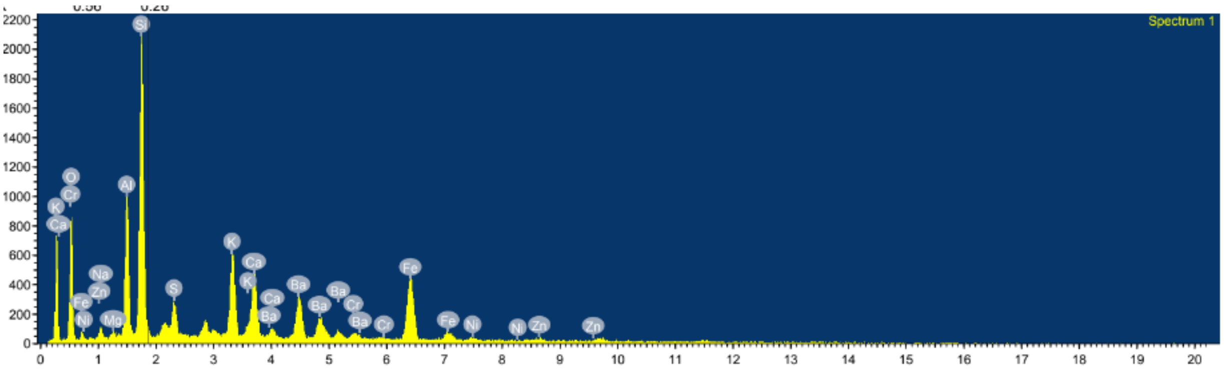

(b)

Figure 29: Pad surface chemistry of sample 3 (a) before (b) after friction test

Besides SEM, PLM (Polarized light Microscopy) was used to further study the porosity present on the rotor surface. As shown in figure 30, rotor sample 1 has the highest porosity represented by the black dots whereas rotor sample 3 has less porosity. The grooves starting from each porous pit indicate the presence of $Cr_{23}C_6$ (chromium carbide) on the rotor surface. They are hard in nature and presence of groove on the rotor surface confirms the abrasive nature of $Cr_{23}C_6$ on the rotor surfaces. The chemical reaction occurring on the rotor surface is as follows.

$$23\,Cr + 6\,C \longrightarrow Cr_{23}C_6$$

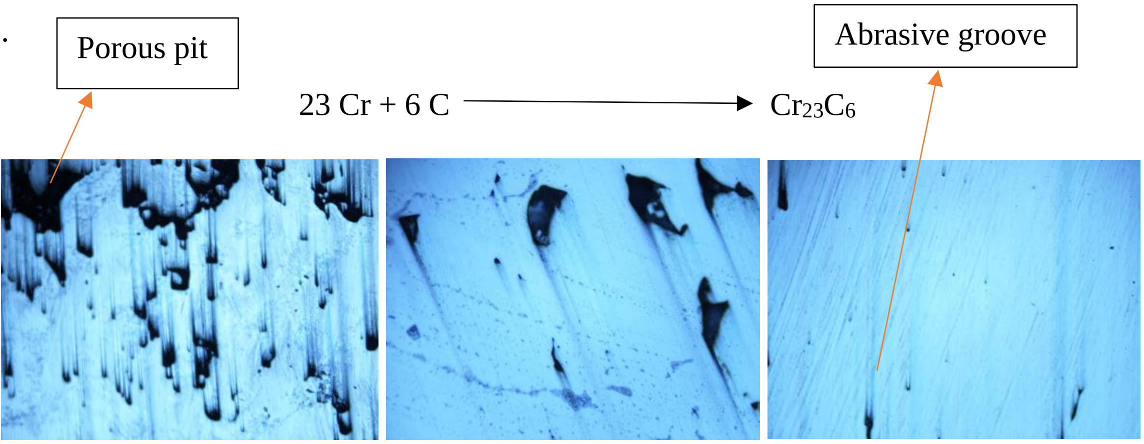

(a) (b) (c)

Figure 30: PLM image of (a) rotor 1 (b) rotor 2 (c) rotor 3

Frequency and amplitude are major factors that are important for analyzing noise. To measure sound or noise level A-weighted filter, and the measurement unit A-weighted decibels, dBA is used. The pressure level of ambient noise varies over time and different statistical characteristics are used to describe the noise variation. LA_{eq} , A-weighted equivalent continuous noise level, is a statistical characteristics that represent a constant sound pressure level which is equivalent to the varying sound level over the measured period of time [40]

Figure 30 shows the noise recorded in dBA during section 4.5, which is the noisiest section among the SAE J2522 section. The blue lines in the figure 30 represents the LA_{eq} value over the period of time. The maximum noise level during this section is over 100 dBA and the minimum noise level is 49 dBA. Occasional Safety and Health Administration (OSHA) standards state that a person exposed to the noise of around 100 dBA for a 2-hour period will reach 100 % of their daily noise dose [3]. Therefore, we can conclude that the SS316 rotor gives noisy braking with an equivalent noise level of 87 dBA. Hence, ear plugs are highly recommended while friction testing on UMT. Research by Singireddy et al. [3], studies the noise generated by cast iron rotor and NAO brake pads during friction test and found the peak noise above 100 dBA during section 4.5 of SAEJ 2522 procedure. This indicates that even cast-iron rotors do not provide less noisier braking.

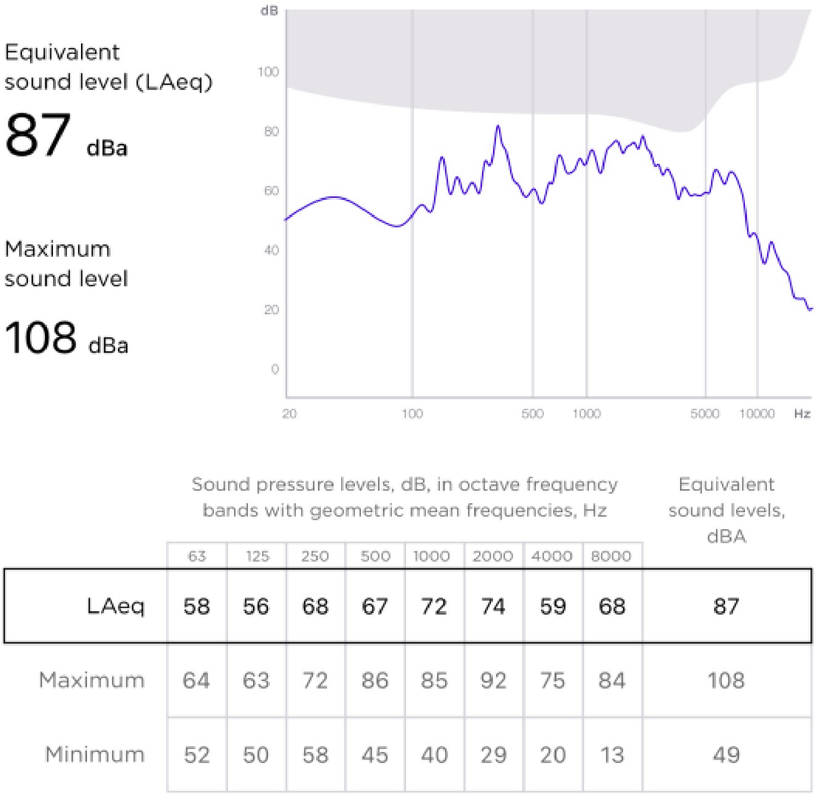

Equivalent sound level (LAeq)

87 dBa

Maximum sound level

108 dBa

	Sound pressure levels, dB, in octave frequency bands with geometric mean frequencies, Hz								Equivalent sound levels, dBA
	63	125	250	500	1000	2000	4000	8000	
LAeq	58	56	68	67	72	74	59	68	87
Maximum	64	63	72	86	85	92	75	84	108
Minimum	52	50	58	45	40	29	20	13	49

Figure 31: Noise during section 4.5 speed/pressure 200-170 kph, 100 ºC, 80 bar for sample.

CHAPTER 5

CONCLUSION

As friction is systems properties and it heavily depends on the physical properties of the surface in contact. This research demonstrates that the application scaled down friction test, surface analysis techniques like SEM, and EDX, and measurement of physical properties like hardness, density, and porosity helps to evaluate the effectiveness of new friction material.

Among 3 SS316 rotor samples, sample 3 was found to be most effective in terms of stable coefficient of friction and wear rate. Sample 3 have higher bulk density (7.81 g/cm^3) and least porosity (0.047 %) compared to sample 2 which could be responsible for high and stable average COF value as shown in figure 18. Although rotor sample 2 have high surface hardness (63.2) than rotor 3, wear rate of rotor 2, 3 are comparative similar, but pad sample 2 wear most than pad sample 3. This indicates that surface hardness is not only responsible for the wear rate. A study conducted by Moore et al., [41] on the relationship between the abrasive wear resistance, bulk hardness and ferritic materials found a direct linear relationship between abrasive wear resistance and bulk hardness. However, it suggested that the wear resistance is greatly influenced by material microstructure than bulk hardness. SEM results showed that combination of adhesive and abrasive friction mechanism is responsible for the development of the friction layer in rotor surface. Dominantly abrasive mechanism was seen for rotor sample 2 whereas adhesive mechanism was found in rotor sample 1 and 3. Similarly, EDX result shows the material transfer from pad bulk metal to rotor surfaces during friction test. Noise generated during the noisiest section of the friction test was also studied and it was found that the SS316 rotor was noisier with a maximum noise level above 100 dBA making this rotor not suitable for quiet braking.

This research work concludes that:

1. Differences in physical properties like bulk density, porosity, hardness are responsible factors resulting in different friction levels.
2. SS316 rotors are characterized by high and stable friction level even in higher temperature braking conditions like fade 2 as well as in high speed (200- 170 kph) and pressure (10- 80 bars) braking conditions.
3. Both rotor and pad samples perform well in terms of wear, wear of rotors sample 2 and 3 are comparatively same however, higher wear rate is found in pad 2 compared to pad 3 because of abrasive mechanism and lower surface hardness of pad sample 2.
4. SS 316 rotors braking are noisy with maximum noise level above 100 dBA.

It is recommended to further study the NVH characteristics. and the impact of the 3D printing method on braking performance.

REFERENCES

[1] P. Blau, “Compositions, Functions, and Testing of Friction Brake Materials and Their Additives,” ORNL/TM-2001/64, 788356, Oct. 2001. doi: 10.2172/788356.

[2] S. K. Kancharla, *Effect of Humidity and testing strategy on Friction Performance of model brake pads containing Nano-additives*. Southern Illinois University at Carbondale, 2018.

[3] V. R. Singireddy, *Development of New Friction Material for Vehicles with Regenerative Braking Systems*. Southern Illinois University at Carbondale, 2022.

[4] K. Friedrich, *Advances in composite tribology*. Elsevier, 2012.

[5] H. Y. Loken, “Asbestos free brakes and dry clutches reinforced with Kevlar® aramid fiber,” *SAE Transactions*, pp. 2202–2208, 1980.

[6] D. Chan and G. W. Stachowiak, “Review of automotive brake friction materials,” *Proceedings of the Institution of Mechanical Engineers, Part D: Journal of Automobile Engineering*, vol. 218, no. 9, pp. 953–966, 2004.

[7] V. V. Kumar and S. S. Kumaran, “Friction material composite: types of brake friction material formulations and effects of various ingredients on brake performance–a review,” *Mater. Res. Express*, vol. 6, no. 8, p. 082005, May 2019, doi: 10.1088/2053-1591/ab2404.

[8] Y. Ma, G. S. Martynková, M. Valášková, V. Matějka, and Y. Lu, “Effects of ZrSiO4 in non-metallic brake friction materials on friction performance,” *Tribology International*, vol. 3, no. 41, pp. 166–174, 2008, doi: 10.1016/j.triboint.2007.07.004.

[9] K. Sowjanya and S. Suresh, “Structural Analysis of Disc Brake Rotor,” *International Journal of Computer Trends and Technology*, vol. 4, no. 7, 2013.

[10] R. Jogineedi, V. R. Singireddy, S. K. Kancharla, S. S. Salvi, A. Jain, and P. Filip, "Impact of Microstructure and Surface Treatment on Thermal Properties of Gray Cast Iron Brake Rotors," SAE Technical Paper, 2021.

[11] B. M. Girish, K. R. Prakash, B. M. Satish, P. K. Jain, and P. Prabhakar, "An investigation into the effects of graphite particles on the damping behavior of ZA-27 alloy composite material," *Materials & design*, vol. 32, no. 2, pp. 1050–1056, 2011.

[12] V. R. Singireddy, R. Jogineedi, S. K. Kancharla, K. Farokhzadeh, and P. Filip, "On scaled-down bench testing to accelerate the development of novel friction brake materials," *Tribology International*, vol. 174, p. 107754, 2022.

[13] J. Erjavec, "Automotive brakes," *Thomson Delmar Learning*, 2003.

[14] T. Kato and A. Magario, "The wear of aramid fiber reinforced brake pads: the role of aramid fibers," *Tribology transactions*, vol. 37, no. 3, pp. 559–565, 1994.

[15] R. Elliott, "Cast iron technology," 1988.

[16] M. A. Maleque^1, S. Dyuti, and M. M. Rahman, "Material selection method in design of automotive brake disc," in *Proceedings of the world congress on engineering*, 2010.

[17] T. F. Stephenson, A. E. M. Warner, S. Wilson, A. T. Alpas, and P. K. Rohatgi, "Aluminum Hybrid Composites Containing Nickel-Coated Graphite Particulate," *Processing Properties and Applications of Cast Metal Matrix Composites*, p. 337, 1996.

[18] M. K. Yoong *et al.*, "Studies of regenerative braking in electric vehicle," in *2010 IEEE conference on sustainable utilization and development in engineering and technology*, IEEE, 2010, pp. 40–45.

[19] D. Antanaitis and M. Robere, “Braking Systems for High Performance Electric Vehicles-A Design Study,” *SAE International Journal of Advances and Current Practices in Mobility*, vol. 3, no. 2020-01–1612, pp. 922–932, 2020.

[20] S. J. Clegg, “A review of regenerative braking systems,” 1996.

[21] L. De Chiffre, S. Carmignato, J.-P. Kruth, R. Schmitt, and A. Weckenmann, “Industrial applications of computed tomography,” *CIRP annals*, vol. 63, no. 2, pp. 655–677, 2014.

[22] S. Adekanye, R. Mahamood, E. Akinlabi, and G. Owolabi, “Additive manufacturing: the future of manufacturing,” *Materiali in tehnologije*, vol. 51, pp. 709–715, Oct. 2017, doi: 10.17222/mit.2016.261.

[23] K. Rane and M. Strano, “A comprehensive review of extrusion-based additive manufacturing processes for rapid production of metallic and ceramic parts,” *Advances in Manufacturing*, vol. 7, pp. 155–173, 2019.

[24] W. Johnson and H. Kudō, *The mechanics of metal extrusion*. Manchester University Press, 1962.

[25] M. Larsson, U. Lindhe, and O. L. A. Harrysson, “Rapid manufacturing with Electron Beam Melting (EBM)-A manufacturing revolution?,” in *2003 International Solid Freeform Fabrication Symposium*, 2003.

[26] J. Allison, C. Sharpe, and C. C. Seepersad, “A test part for evaluating the accuracy and resolution of a polymer powder bed fusion process,” *Journal of Mechanical Design*, vol. 139, no. 10, p. 100902, 2017.

[27] A. Dass and A. Moridi, “State of the art in directed energy deposition: From additive manufacturing to materials design,” *Coatings*, vol. 9, no. 7, p. 418, 2019.

[28] H. Miyanaji, S. Zhang, A. Lassell, A. Zandinejad, and L. Yang, “Process Development of Porcelain Ceramic Material with Binder Jetting Process for Dental Applications,” *JOM*, vol. 68, no. 3, pp. 831–841, Mar. 2016, doi: 10.1007/s11837-015-1771-3.

[29] I. Gibson, D. Rosen, and B. Stucker, *Additive Manufacturing Technologies: 3D Printing, Rapid Prototyping, and Direct Digital Manufacturing*. New York, NY: Springer New York, 2015. doi: 10.1007/978-1-4939-2113-3.

[30] B. Lu, D. Li, and X. Tian, “Development Trends in Additive Manufacturing and 3D Printing,” *Engineering*, vol. 1, no. 1, pp. 085–089, Mar. 2015, doi: 10.15302/J-ENG-2015012.

[31] A. Joshi and L. M. Jugulkar, “INVESTIGATION AND ANALYSIS OF METAL CASTING DEFECTS AND DEFECT REDUCTION BY USING QUALITY CONTROL TOOLS”.

[32] Q. Wang, G. Qi, G. Zhang, and X. Pu, “Study on Brake Durability Dynamometer Experimental Method for Brake NVH and Wear,” SAE International, Warrendale, PA, SAE Technical Paper 2014-01–2520, Sep. 2014. doi: 10.4271/2014-01-2520.

[33] A. E. Anderson, S. Gratch, and H. P. Hayes, “A New Laboratory Friction and Wear Test for the Characterization of Brake Linings,” SAE International, Warrendale, PA, SAE Technical Paper 670079, Feb. 1967. doi: 10.4271/670079.

[34] A. J. Burkman and F. H. Hishley, “Laboratory Evaluation of Brake Lining Materials,” SAE International, Warrendale, PA, SAE Technical Paper 670510, Feb. 1967. doi: 10.4271/670510.

[35] P. W. Lee, J. Leist, and P. Filip, “Use of Hexagonal Boron Nitride in Automotive Friction Materials,” SAE International, Warrendale, PA, SAE Technical Paper 2010-01–1676, Oct. 2010. doi: 10.4271/2010-01-1676.

[36] S. C. R. Kancharla, "MODEL BRAKE MATERIAL FORMULATIONS AND THEIR TESTING AT DIFFERENT SCALE LEVELS," *Theses*, Dec. 2014, [Online]. Available: https://opensiuc.lib.siu.edu/theses/1571

[37] A. A. Alnaqi, D. C. Barton, and P. C. Brooks, "Reduced scale thermal characterization of automotive disc brake," *Applied Thermal Engineering*, vol. 75, pp. 658–668, Jan. 2015.

[38] X. Li and U. Olofsson, "A study on friction and wear reduction due to porosity in powder metallurgic gear materials," *Tribology International*, vol. 110, pp. 86–95, Jun. 2017, doi: 10.1016/j.triboint.2017.02.008.

[39] A. Devaraju, "A Review on Important Factors Affecting Dry Sliding Friction," *Journal of Surface Science and Technology*, vol. 32, p. 73, Apr. 2017, doi: 10.18311/jsst/2016/7751.

[40] Á. Katalin, "Studying noise measurement and analysis," *Procedia Manufacturing*, vol. 22, pp. 533–538, Jan. 2018, doi: 10.1016/j.promfg.2018.03.078.

[41] M. A. Moore, "The relationship between the abrasive wear resistance, hardness and microstructure of ferritic materials," *Wear*, vol. 28, no. 1, pp. 59–68, Apr. 1974, doi: 10.1016/0043-1648(74)90101-X.

VITA

Graduate School
Southern Illinois University Carbondale

Manisha Upreti

manishaupreti80@gmail.com

Kathmandu University,
Bachelor of Engineering, Mechanical, December 2020.

Thesis Paper Title:
Study of Advanced Friction Material for the Automotive Industry

Major Professor: Dr. Peter Filip